

Stratified flow past a prolate spheroid

Jose L. Ortiz-Tarin,¹ K. C. Chongsiripinyo,² and S. Sarkar^{1,*}

¹*Department of Mechanical and Aerospace Engineering, University of California San Diego, La Jolla, California 92093, USA*

²*Department of Mechanical Engineering, Chulalongkorn University, Bangkok 10330, Thailand*



(Received 23 April 2019; published 25 September 2019)

The effect of ambient stratification on flow past a prolate spheroid is investigated using large-eddy simulation. The aspect ratio of the body is $L/D = 4$ and the major axis (L) is aligned with the incoming flow. The Reynolds number based on the minor axis (D) and the incoming velocity (U) is $Re = 10^4$. The stratification is set using a linear density background with constant buoyancy frequency (N). Three simulations with stratification levels, $Fr = U/ND = 0.5, 1, 3$ and one unstratified simulation, $Fr = \infty$, are performed. The influence of the body slenderness ratio is assessed by comparing the present results with previous work on a sphere. An overall result is that the flow past a slender body exhibits stronger buoyancy effects relative to a bluff body. At $Fr \sim O(1)$, there is a strong interaction between the body-generated internal gravity waves (IGW) and the flow at the body. This interaction gives rise to a critical Froude number, $Fr_c = L/D\pi$, which is proportional to the aspect ratio. When $Fr \approx Fr_c$ boundary layer separation is delayed and wake turbulence is strongly suppressed. If $Fr \gtrsim Fr_c$, wake turbulence is only partially suppressed and, when $Fr \lesssim Fr_c$, boundary layer separation is promoted and turbulence reappears. To elucidate the effect of body slenderness on stratification effects, the IGW field, the boundary layer evolution and separation are studied. Analysis of the wake reveals the strong influence of the type of separation, and therefore the body shape, on the dimensions and the energetics of the near and intermediate wake. However, the decay rate of the stratified wake in the nonequilibrium region is the same as that of a sphere.

DOI: [10.1103/PhysRevFluids.4.094803](https://doi.org/10.1103/PhysRevFluids.4.094803)

I. INTRODUCTION

Flow over slender bodies has been extensively studied due to its wide applicability to aerospace and marine engineering. As a canonical, well-defined geometry for flow past three-dimensional objects, the prolate spheroid has received much attention. Special focus has been given to flow separation at different angles of attack [1–3] and the structure of near-body flow [4–6]. Although slender bodies are commonly operated underwater, where the environment has density stratification, fundamental investigations of buoyancy effects on translating objects have neglected slender bodies for the most part. Stratification induces changes in the flow such as the appearance of coherent structures, the generation of internal gravity waves, and alteration in the level and spatial distribution of wake turbulence. This motivates the present computational study of stratified flow past a prolate spheroid. In this work, we examine the influence of the body slenderness on buoyancy effects by comparing our results with previous studies on stratified flow past spheres. To do so, the aspect ratio of the spheroid is set to $L/D = 4$ and the stratification level is increased systematically.

*sarkar@ucsd.edu

Most of the past work on stratified flow past translating bodies has addressed the wake of bluff bodies as reviewed by Lin and Pao [7] and Spedding [8]. The wake of a body with characteristic vertical length D that translates with speed U in a stable background with buoyancy frequency N is governed by the Froude number, $Fr = U/ND$, and the Reynolds number, $Re = UD/\nu$, where ν is the kinematic viscosity of the ambient fluid. Once buoyancy effects have set in, the defect velocity U_d in stratified wakes is larger than in unstratified wakes. Owing to this feature, stratified wakes are said to have a “longer lifetime” relative to their unstratified counterpart. It is worth noting that, even in the case of a weakly stratified environment ($Fr \gg 1$), the local wake Froude number, $Fr_d = U_d/NL_V$, based on the mean values of the defect velocity (U_d) and vertical size (L_V) at a given downstream distance, will eventually approach $O(1)$. Therefore, a stratified wake always differs from its unstratified counterpart at a sufficient downstream distance or, equivalently, after sufficient time (Nt) has passed.

Based on the competition of buoyancy forces with inertial forces, three wake regimes can be distinguished in the evolution of high- Fr wakes [9]: a 3D regime until $Nt = x/D\text{Fr} \approx 2$, where the wake is unaffected by buoyancy and behaves as an unstratified wake, a nonequilibrium regime, where buoyancy forces start suppressing vertical motions and the wake height stops increasing, and, finally, after $Nt = x/D\text{Fr} \approx 50$ (a point that likely occurs further downstream at high Re [10,11]), a quasi-two-dimensional regime where buoyancy forces dominate the flow, and the flow organizes into pancake eddies. In the transition from the 3D regime to the nonequilibrium regime, $Nt = x/D\text{Fr} \approx \pi$ marks an important transition point where Pal *et al.* [12] found oscillatory modulation of the wake. The oscillatory modulation induced by the lee wave results in a transition from the usual decrease of the defect velocity to an increase in $Fr = O(1)$ wakes.

Until recently, when body-inclusive direct numerical simulations (DNS) have become feasible, experiments and temporal simulations were the only available tools to study the near-to-far wake transition in stratified flow. In temporal simulations, the wake generator is not included in the domain and a reference frame that moves with the mean flow velocity is used. The streamwise variations of the mean flow are assumed to be negligible and periodic boundary conditions are imposed so that the cost of the simulation can be reduced. After the early work reviewed by Lin and Pao [7], there was a hiatus followed by experimental investigations of sphere wakes by Spedding [9] and Bonnier and Eiff [13]. The former identified the three regimes with different power laws for the wake decay and the latter observed a “collapse” where the defect velocity exhibited a short interval of increase (now understood as a manifestation of lee-wave induced “oscillatory modulation”). During the same period, Gourlay *et al.* [14], in the first temporal DNS of a stratified wake, found that pancake vortices emerge in the late wake independent of the initial conditions and, Dommermuth *et al.* [15] developed an improved method to initialize the temporal model of large-eddy simulation (LES) and further characterize the wake. Some years later, Brucker and Sarkar [10] conducted temporal DNS at Re up to 5×10^4 and, besides characterizing differences between self-propelled and towed wakes, described buoyancy and internal wave effects on wake evolution in the framework of mean and turbulence energetics. At the same time, Diamessis *et al.* [11] employed implicit LES to characterize wake evolution over a broad range of Froude ($2 < Fr < 32$) and Reynolds ($5 \times 10^3 < Re < 10^5$) numbers. The nonequilibrium regime was found to last longer as Re increases by both Brucker and Sarkar [10] and Diamessis *et al.* [11], and the latter identified secondary KH instabilities that led to turbulence at large Nt . De Stadler and Sarkar [16] found that, in the temporal model, the addition of moderate excess momentum to a momentumless wake led to quantitative but not qualitative changes. Redford *et al.* [17] studied high- Fr wakes and utilized energy budgets to further clarify the change of wake decay induced by stratification.

Body-inclusive spatially evolving simulations of the stratified turbulent wake, like the ones employed in this work, are recent, e.g., Refs. [12,18–20], and have been limited to flow past a sphere. The study by Orr *et al.* [18] at $Re = 200$ and 1000 found that neither the internal waves nor the drag increment due to stratification exhibited significant dependence on Re . Pal *et al.* [19] conducted DNS in the strongly stratified regime ($0.025 \leq Fr \leq 1$) and showed that the usual suppression of turbulence with increasing stratification in flow past a sphere is followed by reappearance of

fluctuations in the near wake when $Fr < 0.5$. The fluctuations in these highly stratified wakes are even more energetic than in their unstratified counterpart. Further examination of the enstrophy and its balance in these $Fr < 0.5$ wakes by Chongsiripinyo *et al.* [20] revealed 3D vortex dynamics as well as dominance of vortex stretching that confirmed the turbulent nature of the fluctuations. The value of $Re = 3700$ in this DNS was higher than the Reynolds number in previous laboratory measurements of low- Fr flow over a sphere that did not show the reappearance of turbulence.

The role of the wake-generator shape in modifying the downstream evolution of stratified wakes has received little attention. An exception is the experimental study by Meunier and Spedding [21] of stratified wakes at moderately high Fr . The work concludes that, far from the body, scaling laws of wakes generated by different body shapes can be collapsed when the shape-dependent drag coefficient is taken into account. In their experiments, the memory loss of initial conditions and the universality of wake decay were only observed in the far wake, where the flow dependence on Fr is partially lost and the local Froude number (Fr_d) governs the evolution. In the present work, however, we wish to ascertain buoyancy effects on the establishment of the near and the intermediate wake that could conceivably depend on the shape of the wake generator.

The stratified flow at and near bodies has also received some attention. Hanazaki [22] conducted the first DNS of stratified flow past a sphere. This DNS, conducted for laminar flow at $Re = 200$, provided visualizations that revealed the imprint of body-generated lee waves on flow separation and the near wake. The drag increase experienced by the body when moving in a stratified environment was quantified, and flow transition to a quasi-two-dimensional regime when $Fr \ll 1$ was observed. Following this computational work, Lin *et al.* [23] and Chomaz *et al.* [24,25] reported results from experimental studies of flow past a sphere where the separation topology was found to change qualitatively in $\{Fr, Re\}$ phase space. Additional work on stratified flow past bodies has been done using bottom-mounted 3D obstacles. This work, motivated by the importance of flow-topography interactions in the atmosphere and the ocean, has also revealed the significance of lee waves in flow separation at $Fr = O(1)$, e.g., Refs. [26,27].

Finally, the generation of body generated lee waves in stratified flow over bodies has also been the subject of much study. Voisin [28] continued previous asymptotic theory [29–32] and applied the Green’s function method to the generation of internal gravity waves by a moving point mass source in a weakly stratified environment with $Fr \ll O(1)$. In followup studies like Dupont and Voisin [33] and Voisin [34], the specific example of internal waves generated by a sphere is described for both $Fr \ll O(1)$ and $Fr \gg O(1)$ regimes, and the variation of drag coefficient with Fr is obtained theoretically. It is worth noting that not only the body but also the turbulent wake generates internal waves [35–40].

The considerable body of work on stratified flow past spheres has led to much of our present understanding of buoyancy effects parametrized by $Fr = U/ND$. Slender bodies have two length scales, the major axis (L) and the minor axis (D), so that flow past a slender body (oriented with D perpendicular to the flow) may not have the same Fr dependence as flow past a sphere, particularly in the near and intermediate wake. In the present work, we consider the specific case of a prolate spheroid to assess the influence of the aspect ratio $L/D > 1$ on the effects of buoyancy in the flow. We will explore the following issues: (1) body-generated internal gravity waves, (2) surface forces, (3) confinement effects, (4) evolution of the boundary layer, (5) flow separation, and (6) near and intermediate wake. The overarching question is how are buoyancy effects different in the case of flow past a slender body with respect to a sphere?

II. PROBLEM FORMULATION

Figure 1 shows the prolate spheroid and the structure of the unstratified wake. The flow is simulated by numerically solving the three-dimensional filtered Navier-Stokes equations in cylindrical coordinates together with a transport equation for density. The coupling between momentum conservation and density transport is simplified using the Boussinesq approximation. A 4:1 aspect ratio prolate spheroid with major axis, L , and minor axis, D , is immersed in a flow

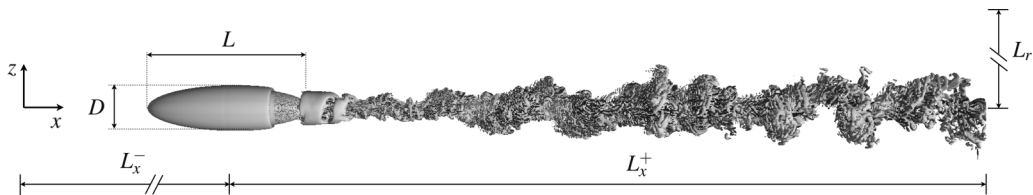


FIG. 1. Isocontour of $Q = \frac{1}{2}|\boldsymbol{\Omega}^2 - \mathcal{S}^2| = 0.1$ at $\text{Fr} = \infty$ to visualize the unstratified wake. Here, $S_{ij} = \frac{1}{2}(\partial u_i/\partial x_j + \partial u_j/\partial x_i)$ is the strain-rate tensor and $\Omega_{ij} = \frac{1}{2}(\partial u_i/\partial x_j - \partial u_j/\partial x_i)$ is the rate of rotation tensor.

with velocity, U , that is aligned with the major axis of the body. The cylindrical coordinate system (r, Θ, x) is transformed to Cartesian (x, y, z) when necessary to simplify the discussion. In both systems, the x coordinate is aligned with the incoming flow, z (vertical) is aligned with gravity, and y (horizontal) with $\Theta = 0$.

The density field is split into the background (constant plus a linear variation) and a density deviation: $\rho(\mathbf{x}, t) = \rho_0 + \rho_l(z) + \rho_d(\mathbf{x}, t)$, where $\rho_l = Cz$ corresponds to linear stable stratification. Typically, $\rho_d/\rho_0 \ll 1$ and $\rho_l/\rho_0 \ll 1$, which leads to the Boussinesq simplification of the momentum equation. The Reynolds number is $\text{Re} = UD\rho_0/\mu$ and the Froude number is $\text{Fr} = U/ND$, where $N = \sqrt{-gC/\rho_0}$ is the buoyancy frequency. The ratio between momentum and density diffusion coefficients, denoted by the Prandtl number ($\text{Pr} = \mu/\kappa$), is set to one instead of $\text{Pr} = 7$, the typical value for temperature diffusion in water. de Stadler *et al.* [41] showed that this change of Pr had a negligible effect on wake statistics and, by setting $\text{Pr} = 1$, the computational cost of the simulations can be significantly reduced. In the LES model, $\text{Pr}_{\text{sgs}} = \mu_{\text{sgs}}/\kappa_{\text{sgs}} = 1$.

The nondimensional governing equations are as follows:

$$\frac{\partial u_i}{\partial x_i} = 0, \quad (1)$$

$$\frac{\partial u_i}{\partial t} + u_j \frac{\partial u_i}{\partial x_j} = -\frac{\partial p}{\partial x_i} + \frac{1}{\text{Re}} \frac{\partial}{\partial x_j} \left((1 + \mu_{\text{sgs}}) \frac{\partial u_i}{\partial x_j} \right) - \frac{\rho_d}{\text{Fr}^2} \delta_{i3}, \quad (2)$$

$$\frac{\partial \rho}{\partial t} + u_j \frac{\partial \rho}{\partial x_j} = \frac{1}{\text{Re Pr}} \frac{\partial}{\partial x_j} \left((1 + \kappa_{\text{sgs}}) \frac{\partial \rho}{\partial x_j} \right). \quad (3)$$

Henceforth, u_i , x_i , p , and ρ will denote nondimensional quantities. For nondimensionalization, the incoming streamwise velocity U is used as the velocity scale and the minor axis D is used as the length scale. Here, p is the nonhydrostatic pressure, nondimensionalized with $\rho_0 U^2$. In Eq. (2) and Eq. (3), μ and κ have been used to nondimensionalize the subgrid diffusion coefficients, μ_{sgs} and κ_{sgs} . The subgrid diffusion coefficients are computed using the dynamic eddy viscosity model proposed by Germano *et al.* [42] and improved by Lilly [43]. This LES closure estimates the Smagorinsky coefficient by dynamically filtering the flow field with a coarse test filter. By doing so, the contribution of the resolved stresses to the test filter scales can be estimated together with a Smagorinsky constant. This closure has been broadly used and it reproduces the correct behavior in laminar regions, high-shear regions, and near walls when enough points are used in the boundary layer.

Boundary conditions suitable for this problem are

$$u = U, \quad v = w = p = 0, \quad \rho = \rho_0 + \rho_l \quad \text{at the inlet}, \quad (4)$$

$$\partial_t \mathbf{u} = U \partial_x \mathbf{u}, \quad \partial_x p = 0, \quad \rho = \rho_0 + \rho_l \quad \text{at the outlet}, \quad (5)$$

$$\lim_{r \rightarrow 0} \partial_\theta \mathbf{u} = 0, \quad \lim_{r \rightarrow 0} \partial_\theta p = 0, \quad \lim_{r \rightarrow 0} \partial_\theta \rho = 0 \quad \text{on axis}, \quad (6)$$

TABLE I. Simulation parameters. The value of Fr is changed among cases by changing N .

Case	Re	Fr	L_r	L_θ	L_x^-	L_x^+	N_r	N_θ	N_x
1	10^4	∞	10	2π	10	18.5	830	128	5120
2	10^4	3	60	2π	33	30	600	128	5120
3	10^4	1	60	2π	33	30	600	128	5120
4	10^4	0.5	60	2π	33	30	600	128	5120

$$\partial_r \mathbf{u} = 0, \quad \partial_r p = 0, \quad \partial_z \rho = C \quad \text{at the lateral wall,} \quad (7)$$

$$\mathbf{u} = 0, \quad \partial_n p = 0, \quad \partial_n \rho = 0 \quad \text{on the body surface,} \quad (8)$$

and periodicity in the azimuthal direction for all the variables.

III. NUMERICAL METHOD AND VALIDATION

The governing equations are discretized with finite differences on a cylindrical staggered grid. The solver advances in time using a fractional step method that combines a third-order low storage Runge-Kutta method for the convective terms with Crank-Nicolson for the viscous terms. The implicit treatment alleviates the stiffness of the system, especially due to the small $r\Delta\Theta$ values near the axis. The use of cylindrical coordinates has two main advantages. First, the periodicity of the domain can be leveraged to reduce the cost of solving the pressure Poisson problem. The periodic condition in the azimuthal coordinate reduces the discretized Poisson equation to a pentadiagonal system that is solved using a direct solver [44]. Second, the cylindrical topology of the grid is an appropriate choice for the axisymmetric surface of the body, the boundary layer, and the high shear regions in the wake.

The body is represented as a forcing term in the right hand side of the equations with the immersed boundary method introduced by Balaras [45] and Yang and Balaras [46]. To enforce the wall boundary conditions, the force exerted by the body on the fluid is interpolated from the body surface to the adjacent fluid points at every time step.

To avoid spurious reflection of the waves, a sponge layer is introduced in the inlet, the outlet, and the lateral wall of the domain. The sponge takes the form of a Rayleigh damping function given by $\phi(\mathbf{x})(\mathbf{u} - \mathbf{U})$ and $\phi(\mathbf{x})[\rho(\mathbf{x}) - \rho_{bg}(z)]$, where $\mathbf{U} = (U, 0, 0)$ is the freestream velocity and $\rho_{bg} = \rho_0 + \rho_l(z)$ is the background density. The sponge strength, ϕ , is given by a quadratic profile that gradually relaxes the velocities and the density to their respective values at the boundaries.

The Reynolds number based on the minor axis is set to $\text{Re} = 10^4$, which corresponds to $\text{Re}_L = UL/\nu = 4 \times 10^4$. Four cases, which are listed in Table I, are simulated with different levels of stratification $\text{Fr} = 0.5, 1, 3$ and the unstratified $\text{Fr} = \infty$. The numerical method has been well-validated in flow past a sphere at $\text{Re} = 3700$ [12,19,20] by comparing results against existing simulations and experimental data. Here, the grid validation is performed by comparing the pressure coefficient, C_p , and the friction coefficient, C_f , with Wang [1]. To the authors' best knowledge, this is the only detailed work to investigate flow over a 4:1 spheroid at zero angle of attack and moderately high Reynolds number. Wang [1] resolves the boundary layer equations in spheroidal coordinates using the potential solution by Lamb [47] as a matching outer boundary condition.

Figure 2 compares the results of Wang [1] with the current unstratified simulation, where C_p and C_f are defined as

$$C_f = \text{sgn}\tau_1 \frac{|\tau_i|}{\frac{1}{2}\rho_0 U^2}, \quad C_p = \frac{p}{\frac{1}{2}\rho_0 U^2}. \quad (9)$$

Here, $\tau_i = \mu(\frac{\partial u_i}{\partial x_j} + \frac{\partial u_j}{\partial x_i})n_j$ is the wall shear stress with n_j the unitary vector normal to the surface.

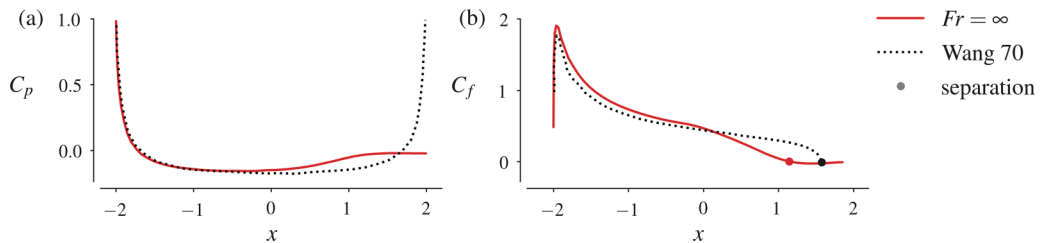


FIG. 2. Comparison of the unstratified numerical simulation with the result of Wang [1] who matches a boundary-layer solution with the outer potential flow: (a) pressure coefficient and (b) friction coefficient and separation point.

The solid red curve in Fig. 2(a) compares the streamwise evolution of C_p with the potential-flow solution used to prescribe pressure by Wang [1]. Figure 2(b) represents the streamwise evolution of the surface friction coefficient where C_f is normalized by the viscous length scale $D/\text{Re}^{1/2}$ to obtain $O(1)$ values. The location of the separation point, where $C_f = 0$, is also shown. In the present simulation, the initial pressure is not recovered at the stern of the body due to the viscous losses at the wall and in the separated flow. This effect cannot be captured in Wang [1] because of the one-way coupling between the potential-flow solution and the boundary layer equations.

To further assess the quality of the grid, the ratio of the grid spacing to the Kolmogorov length scale is computed in each direction. The Kolmogorov length is defined as $\eta = (\nu^3/\varepsilon)^{1/4}$. The turbulent dissipation rate, ε , is computed as $\varepsilon = 2\nu\overline{S'_{ij}S'_{ij}}$, where S'_{ij} is the fluctuating strain-rate tensor. The present LES has high resolution. As Fig. 3 shows, the ratio of the radial and streamwise grid spacing to η is <2 , and the ratio of the azimuthal grid spacing to η is <6 . Indeed, apart from the azimuthal grid spacing, the simulation has a DNS-like resolution. Within the boundary layer, there are 47 grid points at $x/L = 0.25$ (measured from the nose), 71 at $x/L = 0.5$, and 100 at $x/L = 0.75$. This is more than sufficient to establish good resolution of boundary-layer dynamics.

IV. VISUALIZATION

A three-dimensional view of the unstratified wake was provided in Fig. 1. To reveal the effect of stratification on the wake, instantaneous vorticity fields are shown in Fig. 4 (vertical plane) and

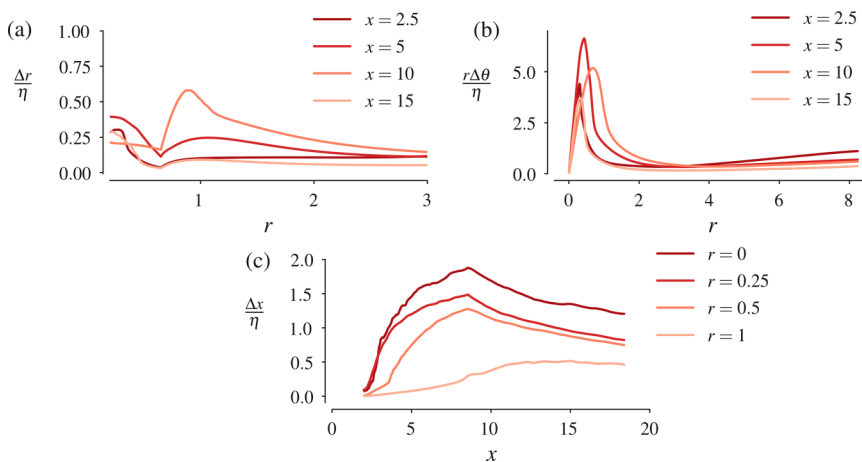


FIG. 3. Grid size scaled with the Kolmogorov length η in the unstratified case: (a) radial size, (b) azimuthal size, and (c) streamwise size.

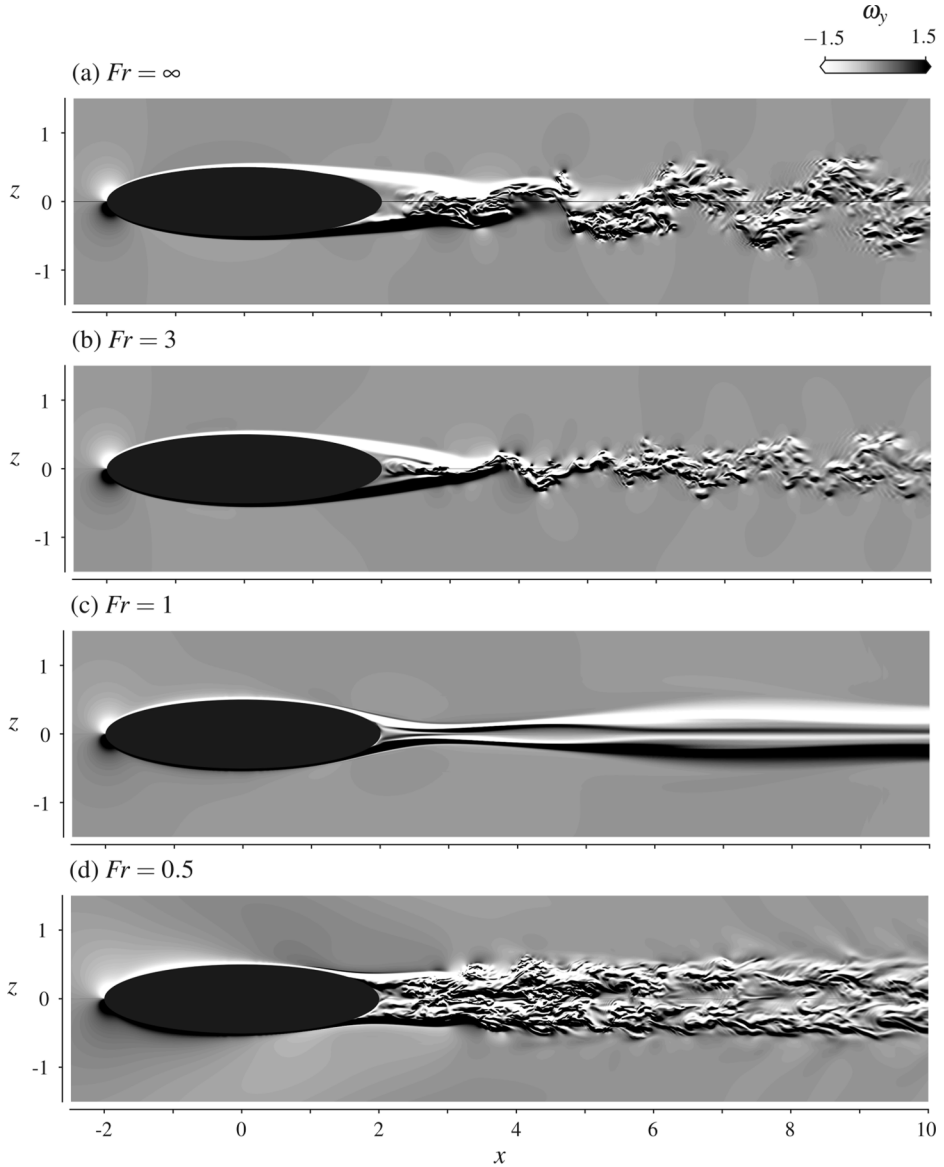


FIG. 4. Effect of Fr on the instantaneous lateral vorticity ω_y in the vertical plane.

Fig. 5 (horizontal plane) for four different Froude numbers. The visualization of vorticity clearly reveals the main characteristics of the flow: the growth of the boundary layer, the separation, the breakdown of the separated shear layer, and the generation of turbulent structures in the wake. As the stratification level is increased, the suppression of turbulent structures is progressively stronger, eventually leading to the development of a completely laminar wake at $Fr = 1$; see Figs. 4(c) and 5(c). When stratification is further increased to $Fr = 0.5$, turbulence reappears in the wake as shown by the fine-scale features in Fig. 4(d). This behavior differs from that of a sphere. The sphere at $Re = 10^4$ and $Fr = 1$ has a turbulent wake [48] and, at $Fr = 0.5$ and $Re = 3700$ [19], a fully laminar wake. (Note that the sphere Re is based on the diameter, which is consistent with the current definition based on the minor axis of the prolate spheroid.)

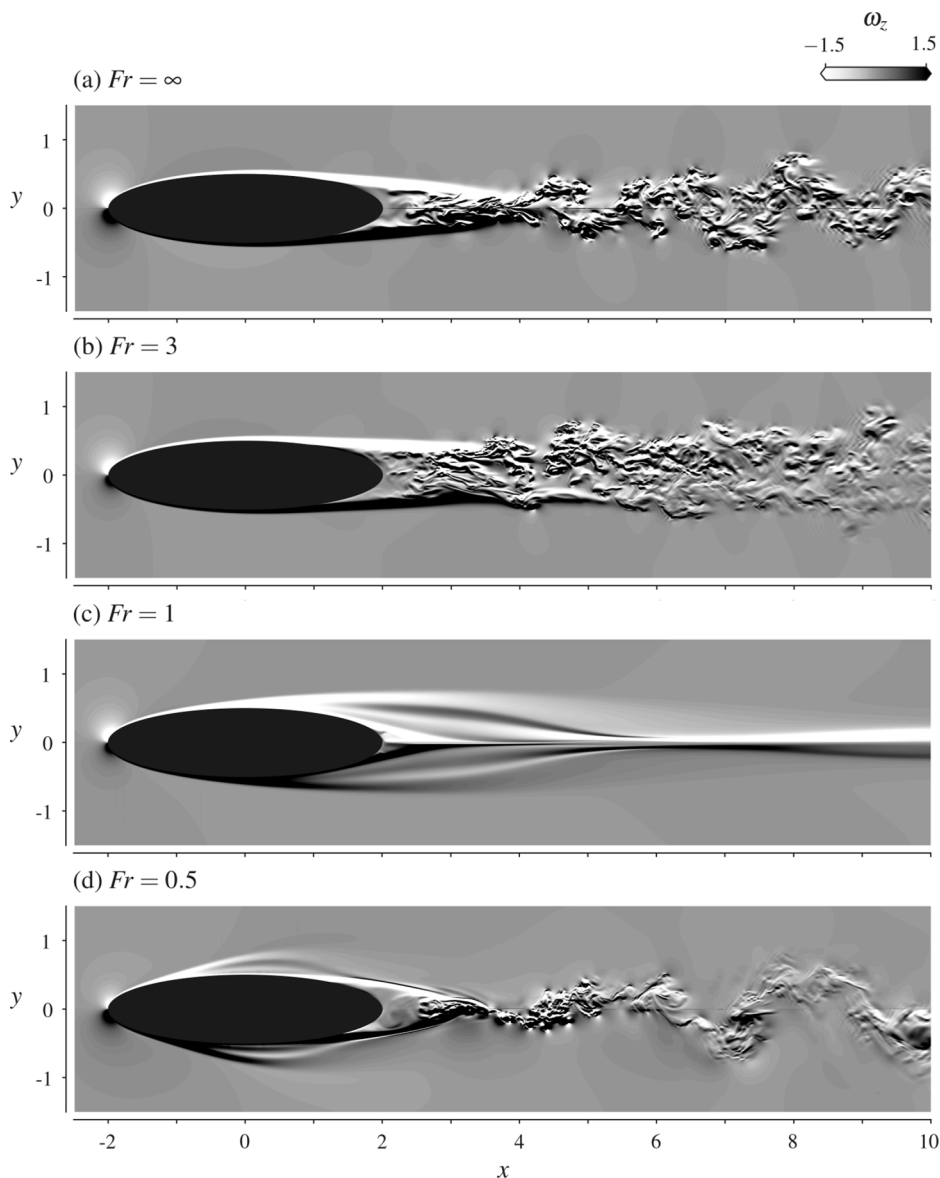


FIG. 5. Effect of Fr on the instantaneous vertical vorticity ω_z in the horizontal plane.

The unstratified case [Figs. 4(a) and 5(a)] shows an axisymmetric separated shear layer in the aft of the body. The shear layer, identified by the intense white and black vorticity stripes, is unstable and triggers the emergence of a coherent helical mode in the wake (Fig. 1). The inclusion of a vertical density gradient breaks the axial symmetry of the problem. The weakly stratified $Fr = 3$ case shows a flattened recirculation region. Comparison of Figs. 5(b) and 4(b) reveals a turbulent region whose width is larger than its height. Thus gravity has reduced the height of the recirculation bubble and has accelerated the vertical contraction of the shear layer. This characteristic azimuthal anisotropy is also observable in the near wake, which remains more wide than tall.

The strongly stratified $Fr = 1$ case is steady. The near wake is "locked in" by the lee wave and no unsteadiness develops in the aft of the body. Its vorticity field displays a triple-layered structure in

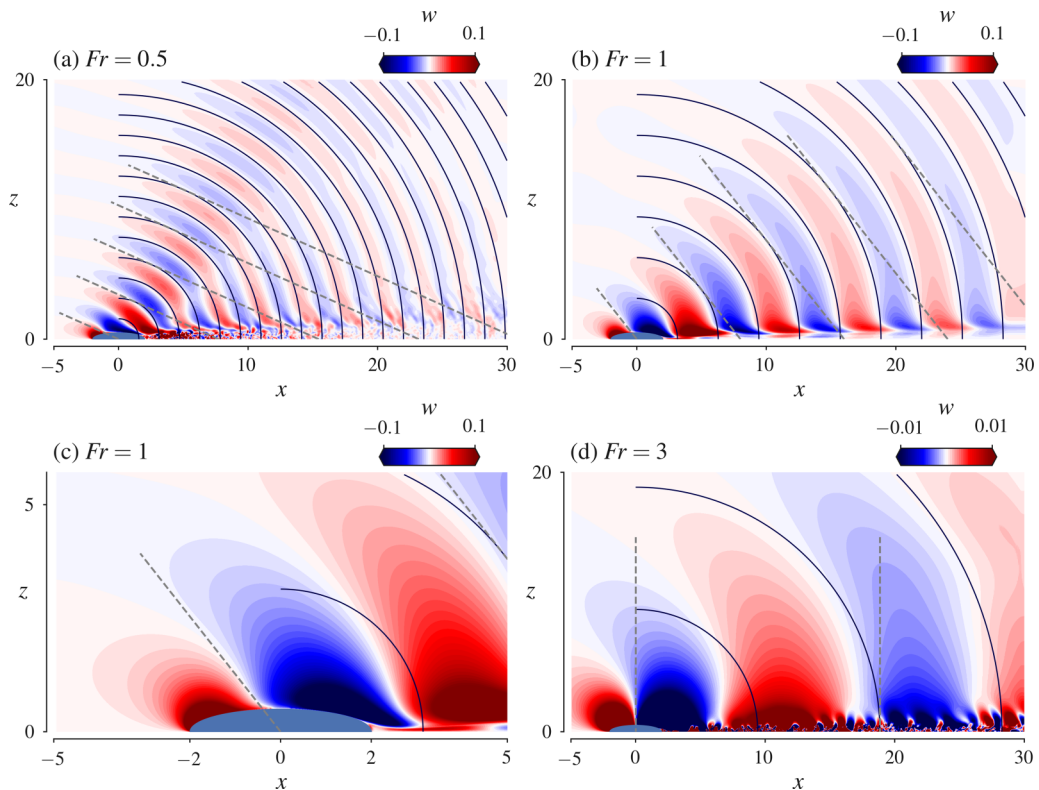


FIG. 6. Internal gravity waves, visualized by contours of vertical velocity (w): (a) $Fr = 0.5$, (b) $Fr = 1$, (c) a zoom of $Fr = 1$ to highlight the inclined phase lines on the body, and (d) $Fr = 3$. The black solid lines in each panel represent the $w = 0$ phase lines obtained with the asymptotic theory for the far field; see Eq. (11). The gray dashed lines in each panel mark the phase lines of $w = 0$ obtained by the near-field theory; see Eq. (10).

the vertical plane [Fig. 4(d)] generated by three distinguishable flow regions: the two regions where flow goes above and below the body and the central region where the flow is unable to surmount the body and goes around the sides [25]. Within this region, a horizontal thin shear layer develops [Fig. 5(c)].

At $Fr = 0.5$, the strongest stratification considered here, there is a wider separation region and a taller wake than at $Fr = 1$. Also, there are unsteady small-scale motions in the vertical plane [Fig. 4(c)]. In the horizontal plane, high-vorticity regions are observed at the sides of the body followed by a sinuous wake [Fig. 5(d)].

V. INTERNAL GRAVITY WAVES

The motion of a body in a stratified environment generates internal gravity waves (IGW) that propagate energy and momentum away from the body. These waves are three-dimensional, dispersive, anisotropic, and emitted by multiple sources. The behavior of the IGW is important to understand the influence of stratification on the boundary layer and flow separation to be discussed in later sections.

Figure 6 shows an instantaneous snapshot of vertical velocity in the upper vertical plane at different Froude numbers. A periodic semicircular pattern can be distinguished in panels (a), (b), and (d), where regions of positive and negative velocity alternate. This pattern is steady and generated

by the body lee waves. A less coherent pattern can be observed in the wake region, near the axis ($z = 0$), in panels (a) and (d). These waves are unsteady and are emitted by the fluctuating motions of the wake. Generally, three major contributors to the IGW field can be distinguished: the body, the coherent structures shed from the body, and the wake turbulence [35–37]. In this section, we will describe the steady body-generated lee waves, deferring the analysis of unsteady waves to future work.

A large body of IGW work concerns the geophysical problem of stratified currents moving past topography (mountains, ridges, rough terrain) [49]. Additional work has been done to describe the wave field generated by moving objects, primarily spheres. Section V A explores the similarities between the flow past a slender body and flow over corrugated topography to describe the IGW near field. Section V B adapts the work of Voisin [34] on stratified flow past a sphere to describe the IGW far field generated by a slender body. Both sections aim to elucidate theoretically the role of aspect ratio on the wave field.

A. Near-field theory

Close inspection of the wave field near the body (Fig. 6) reveals a characteristic tilt of the IGW that depends on the Froude number. This tilt is clearly observed on the phase line which intersects the spheroid surface and in those closest to the body, as illustrated by Fig. 6(c). However, the tilt becomes less pronounced as we move away from the origin [Figs. 6(a), 6(b), and 6(d)]. The tilt angle of the near-body phase lines can be estimated by drawing an analogy between the flow past a three-dimensional spheroid and the two-dimensional flow over a surface corrugation. This analogy has proved useful in the context of stratified flow over three-dimensional ridges [50,51].

A stratified flow over a surface corrugation of wave number k_s generates an IGW field that has the same characteristic wave number k_s . This is one of the simplest configurations where IGW develop and only a single dominant frequency appears. The IGW shows straight phase lines tilted an angle θ from the vertical. In a case where the size of the body is finite, such as the flow past a two- or three-dimensional ridge of finite width L , a full spectrum of wave numbers is generated, not just $k_s = 2\pi/L$. However, k_s remains the dominant wave number. In this case, the IGW cannot be simply described as a monochromatic wave, although the fundamental physics remain unchanged [52] and the angle estimation is still relevant.

To elucidate the role of the aspect ratio on the tilt, the phase lines generated by a corrugated topography of wavelength $\lambda_s = 2L$ are plotted on top of the simulation results in Fig. 6. They form an angle θ with the vertical where

$$\frac{\omega}{N} = \cos \theta \Rightarrow \cos \theta = \frac{\pi U}{LN} = \frac{\pi Fr D}{L}, \quad (10)$$

and $\omega = \pi U/L$ is the frequency measured by an observer moving with the flow. Equation (10) is the dispersion relation obtained by assuming that the body generates a small-amplitude periodic disturbance. The expression for ω can be obtained by forcing the phase to be constant relative to the moving body [53]. The angle of the IGW phase lines (θ) also describes the direction at which energy is radiated from the body. As shown by Eq. (10), θ depends not only on Fr but also explicitly on the body aspect ratio. Figure 6(c) shows that the inclined straight phase line obtained from Eq. (10) agrees well with the simulated waves near the body. The effect of changing the Froude number is shown by Figs. 6(a) and 6(d). In the Fr = 0.5 configuration, θ increases and the phase lines are more inclined with the vertical. For the weakly stratified Fr = 3 case, where Fr > $L/D\pi$, the value of $\omega/N > 1$ would indicate that the body-generated waves cannot be sustained in the far field. Instead, there is a decaying solution corresponding to evanescent waves whose energy is trapped near the body and exponentially decays with height. The simulation reveals the existence of very weak waves whose phase lines are perpendicular to the body in the near field. A similar pattern of perpendicular phase lines is observed in the sphere of Pal *et al.* [12] at Fr = 1 (not shown), where the conditions also correspond to Fr > $L/D\pi$ and $\omega/N > 1$.

Figure 6(c) also shows that the phase lines are more tilted with respect to the vertical inside the wake ($\theta_{\text{wake}} > \theta$), a phenomenon that can also be understood through Eq. (10). The velocity relative to the free stream is reduced in the wake, implying that $\omega_{\text{wake}} < \omega$, and the phase lines near the center line get closer to the horizontal.

The velocity and pressure associated with the IGW near field can influence the boundary layer and flow separation. We will discuss these effects later in Sec. VIC.

B. Far-field theory

Far from the body and in the vertical plane, the IGW field shows a pattern of alternating semicircular stripes of positive and negative radial velocity, as seen in Figs. 6(a), 6(b), and 6(d). The wave number is proportional to the Froude number and the amplitude of these waves decays far from the body as $r^{-1/2}$, in agreement with the experiments of Gilreath and Brandt [35].

Asymptotic analysis has been extensively used [28,31,33,34] to estimate the wave field generated by moving objects. This body of work seeks far-field solutions and considers the regimes of $\text{Fr} \gg 1$ or $\text{Fr} \ll 1$, where nonlinearities can be neglected. The underlying assumption of the far-field theory is that the actual shape of the body loses significance as we move away from it. As such, the body can be substituted by a simpler wave source as long as it generates a similar type of disturbance on the flow field. It should be noted that, even when the exact body shape might not be very significant in the far field, the actual size of the body is relevant (not to the frequency of the far-field waves but, particularly, to their amplitude and the exact location of the phase lines). This is why, even when there are analytical solutions that describe the wave field generated by a sphere, some modifications of these solutions are required to properly describe the IGW generated by a body such as the 4:1 spheroid.

In the formulation of Voisin [28,34] for wave generation by a horizontally moving sphere, a mass source q is included in the right hand side of the continuity equation to model the moving body. This source term can, in general, be either a monopole, a dipole, or a combination of singularities. After further simplifications of the linearized inviscid equations, the system is reduced to a single propagation equation for a wave function χ [54]. The wave function is a scalar function that contains all the wavelike components of the fluid motion, allowing us to simplify the formulation of the problem by excluding all the nonpropagating vortical motions that are not part of the wave field.

The Green's function associated with the internal wave equation for χ can be obtained asymptotically for large times ($N|t| \gg 1$) and integrated in the complex plane for any forcing q using the method of stationary phase [55] as described by Voisin [34]. Once the wave function χ is known, the vertical velocity field can be obtained by differentiation, resulting in $w = \frac{\partial^2}{\partial r^2} \frac{\partial}{\partial z} (\chi)$. Taking into account that only the variations of the phase of χ are significant (to leading order), w in the reference frame moving with the body reads

$$w(\mathbf{x}, t) \sim \frac{N}{2\pi U r} \sin \phi \cos \theta (1 + \cot^2 \theta \cos^2 \phi)^{1/2} \text{Im} \left[iq(\mathbf{k}, t_s) \exp \left(-i \frac{N}{U} r |\sin \phi| \right) \right], \quad (11)$$

where the spherical polar coordinates (r, θ, ϕ) are given by

$$x = r \cos \theta, \quad y = r \sin \theta \cos \phi, \quad z = r \sin \theta \sin \phi, \quad (12)$$

the wave number vector is

$$\mathbf{k} = \frac{N}{U} \left(-\cos \theta |\sin \phi|, \frac{\cos^2 \theta}{\sin \theta} \cos \phi |\sin \phi|, -\frac{\sin^2 \theta + \cos^2 \theta \cos^2 \phi}{\sin \theta} \text{sgnz} \right), \quad (13)$$

and t_s is the time of the source, which, by causality, is always $t_s < t$.

At this point, Eq. (11) can be used to obtain the wave field generated by a spheroid instead of a sphere. To that end, q is chosen to be the sum of two monopoles, a source and a sink, separated by

a distance $2a$, as has been done for a Rankine ovoid [31]. This yields

$$q(\mathbf{x}) = m[\delta(x+a) - \delta(x-a)]\delta(y)\delta(z), \quad (14)$$

which, in Fourier space, is given by

$$q(\mathbf{k}) = 2im \sin(ak_x). \quad (15)$$

Applying Eq. (15) as the forcing $q(\mathbf{k})$ in Eq. (11) gives

$$w(\mathbf{x}, t) \sim -\frac{mN}{\pi U r} \sin \phi \cos \theta (1 + \cot^2 \theta \cos^2 \phi)^{1/2} \sin \left(\frac{Na}{U} \cos \theta |\sin \phi| \right) \sin \left(\frac{N}{U} r |\sin \phi| \right), \quad (16)$$

where a and m can be obtained from the potential solution of the Rankine ovoid by imposing a stagnation point at $x = \pm L/2$ and taking the diameter at $x = 0$ to be D . This yields

$$L = 2a \sqrt{\frac{m}{\pi a U} + 1}, \quad D = 2a \cot \left(\frac{\pi U D}{2m} \right). \quad (17)$$

The strong assumptions required to obtain Eq. (16) are assumed to be valid only at large distances from the source ($r \gg a$) in a weakly stratified environment. However, previous experiments [33] have shown these assumptions to be valid even in the moderately stratified regime, as long as the compactness condition ($a \ll \lambda$ where λ is the wavelength) is met. Figure 6 shows the phase lines for $w = 0$ (black solid lines) obtained from Eq. (16) in the upper vertical plane. The theoretical phase lines agree well with the wavelength and phase of the simulated IGW field.

The steady IGW generated in the lee of the body alters the wake evolution. The effect of the gravity waves on the wake decay will be discussed in Sec. VII.

VI. FLOW AT THE BODY

In addition to enabling gravity waves, stratification affects the flow at the body in two distinct ways: (1) through the interaction of buoyancy force with the body curvature and (2) through vertical confinement and blocking. These buoyancy effects change the surface forces, affect the boundary layer evolution, and, ultimately, the flow separation. This section includes a description of these modifications to the flow.

A. Surface forces

The drag coefficient C_d , a nondimensional measure of the streamwise (x) component of the force, can be split into two contributions: the viscous drag coefficient C_d^f and the pressure drag coefficient C_d^p . Thus $C_d = C_d^p + C_d^f$, where C_d^f accounts for the viscous skin friction and C_d^p accounts for pressure differences over the body surface. The component force coefficients are given by

$$C_d^f = \frac{1}{\frac{1}{2} \rho_0 U^2 \frac{\pi}{4} D^2} \int_S \tau_1 dS, \quad C_d^p = \frac{1}{\frac{1}{2} \rho_0 U^2 \frac{\pi}{4} D^2} \int_S (-p) n_1 dS, \quad (18)$$

where τ_i is the wall shear stress, n_j is the unitary vector normal to the wall, and dS is a surface differential element.

Table II shows the magnitude of the time-averaged force coefficients for the four simulated cases. An averaging window of $\approx 30D/U$ is applied after the flow has reached steady state. The effect of stratification is reported using $\Delta C_d(\text{Fr}) = C_d(\text{Fr}) - C_d(\infty)$ [56,57]. As stratification increases, the drag increases, an effect that has also been found for a sphere at $\text{Re} \sim 10^3$ in the $\text{Fr} = O(1)$ regime [56,58]. As it is expected for a slender body, the major contributor to drag in the unstratified case is the surface friction [59]. However, as the Fr decreases, the contribution of the pressure drag C_d^p due to both internal waves and the wake overcomes the viscous drag and becomes dominant.

TABLE II. Surface forces.

Case	Re	Fr	C_d	C_d^f	C_d^p	ΔC_d
1	10^4	∞	0.161	0.121	0.041	0
2	10^4	3	0.164	0.119	0.045	0.003
3	10^4	1	0.336	0.149	0.187	0.175
4	10^4	0.5	0.647	0.158	0.489	0.486

To understand the effect of stratification on the surface forces, it is useful to look at the streamwise evolution of C_f and C_p [Eq. (9)] shown in Fig. 7. As previously mentioned in the validation section, inviscid theory leads to the following picture for an unstratified flow over an axisymmetric body at zero angle of attack.

The nose of the body ($x = -2$) is a stagnation point where the flow kinetic energy is converted into pressure. During its motion towards the center of the body ($-2 < x < 0$), the fluid accelerates and the kinetic energy recovers at the expense of pressure. Downstream of the central part of the body ($0 < x < 2$), the behavior is inverted, velocity decreases, and pressure rises again. Once we introduce the effect of viscous losses, which cause the recovery of pressure to be partial, the behavior of C_p observed in Fig. 7(a) for unstratified flow can be understood.

Gravity and stratification enter this picture through their effect on the flow acceleration. As shown in Fig. 7(a) most of the pressure drop occurs in the foremost region of the nose, $-2 < x < -1.8$, where the slope of the body is still significant. In this region, the body-tangential component of the gravity vector is maximum and the buoyancy term in the momentum conservation equation has maximum effect on the flow speed. Since the fluid that is transported along and over the body in the vertical plane is denser than the background, the buoyancy term [$\mathbf{b} = -\rho_d/\text{Fr}^2 \mathbf{k}$ in Eq. (2)] is negative (downward) and its body-tangential component acts to reduce the initial increase of velocity. Thus the pressure in the forward portion of the body increases relative to its unstratified counterpart. When the flow reaches the rearward portion of the body, however, the effect is reversed. The restorative buoyancy force acts to increase the flow speed and pressure remains lower than in the unstratified case. Figure 7(a) shows that, relative to $\text{Fr} = \infty$, C_p in the $\text{Fr} = 1$ and $\text{Fr} = 0.5$ cases is larger in the forward portion and smaller in the rearward portion, consistent with the preceding qualitative argument.

Figure 7(b) shows that the azimuthally averaged friction coefficient is also affected by buoyancy in the $\text{Fr} = O(1)$ regime. The aforementioned reduction of flow speed in the frontal region leads to a smaller value of C_f , whereas the enhanced flow speed on the aft increases the skin friction.

To summarize, the effect of buoyancy on the flow acceleration around the body modifies the drag primarily by reducing the overall pressure in the back of the body and increasing the pressure in the front, causing a major increase in C_d^p .

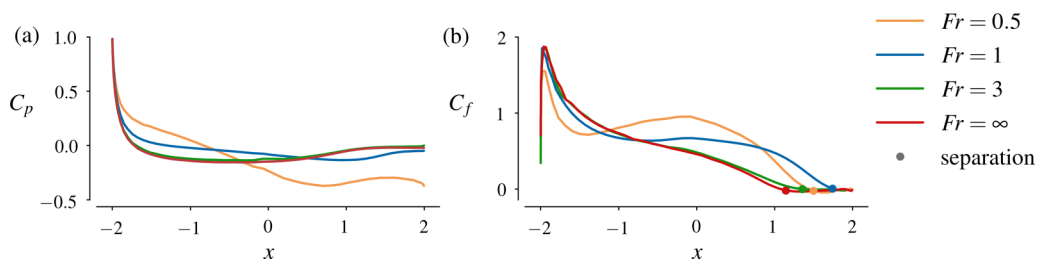


FIG. 7. Effect of Fr on azimuthally averaged force coefficients: (a) pressure coefficient C_p and (b) friction coefficient C_f . The separation point is indicated by dots on the C_f curves.

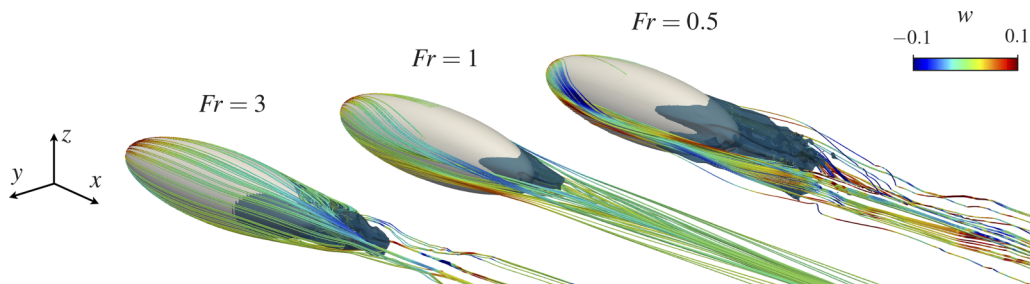


FIG. 8. Effect of Fr on the streamlines starting from the nose of the body. The streamlines are colored by vertical velocity. The blue isosurface in the aft of the body marks the points where the streamwise velocity $u = 0$.

B. Vertical confinement and upstream blocking

Stratification induces upstream blocking whereby a portion of the flow ahead of the body is unable to travel above it and is, instead, diverted to the sides. As such, unlike in the unstratified case, the flow is vertically confined.

Figure 8 shows a group of streamlines that start on the nose of the spheroid. In the weakly stratified case ($Fr = 3$), the streamlines are evenly distributed in the azimuthal direction and their color shows a region of positive vertical velocity at the nose of the body and negative vertical velocity at the aft. The $Fr = 1$ and $Fr = 0.5$ cases show that the streamlines are deflected towards the side of the body instead of going above it. In particular, the $Fr = 0.5$ case shows a large region at the nose of the body where the vertical velocity is negative.

The conditions under which a parcel of fluid can surmount an obstacle is a question of longstanding importance to the stratified-flow community [57,60,61]. To pass above an obstacle, a parcel of fluid in a stratified medium has to overcome a potential energy barrier created by the vertical density gradient. Drazin [61] developed a model for asymptotically low Fr that describes the stratified flow past an obstacle as the sum of two flows: a horizontal flow that, confined by the stratification, goes around the obstacle and a secondary three-dimensional flow that is able to go above/below the obstacle. Based on this model, a separating stream surface that divides the flow that goes around from the flow that goes above the body can be defined. The flow above/below the dividing stream surface is responsible for the generation of waves and the associated wave drag.

The remainder of the flow is blocked and induces the vertical vorticity mode rather than internal gravity waves. According to this theory, the height of the dividing stream surface (z_s) can be estimated using *Sheppard's criterion* as $z_s = (1 - Fr)D$. Although based on asymptotic analysis at $Fr \ll 1$, the theory has proved useful to understand the flow even at the moderate stratification of $Fr = O(1)$.

If mixing of density is neglected, isopycnal surfaces serve as surrogates for stream surfaces. Figure 9 shows the projection of three-dimensional instantaneous isopycnals in the upper vertical plane. The colored isopycnal is the highest isopycnal that is pierced by the body surface and marks the dividing stream surface. The isopycnals in Fig. 9 that originate below the dividing stream surface are unable to surmount the obstacle. Instead, they deflect downward and horizontally away from the boundary of the obstacle, as was shown in Fig. 8. Consider fluid that originates from a region \mathcal{R} that is upstream of the body and within $0 < z < 0.5$. The colored isopycnal, taken to be the vertical $x - z$ -plane projection of the dividing stream surface, splits the fluid that originates in \mathcal{R} into two classes: fluid above the dividing stream surface is able to go above the body while the fluid below does not. Note that, by symmetry, there is a second dividing stream surface in the lower half of the body ($-0.5 < z < 0$) that separates fluid that is able to go below the body from the fluid that does not. Theory predicts that when $Fr \rightarrow \infty$ these two dividing stream surfaces merge into

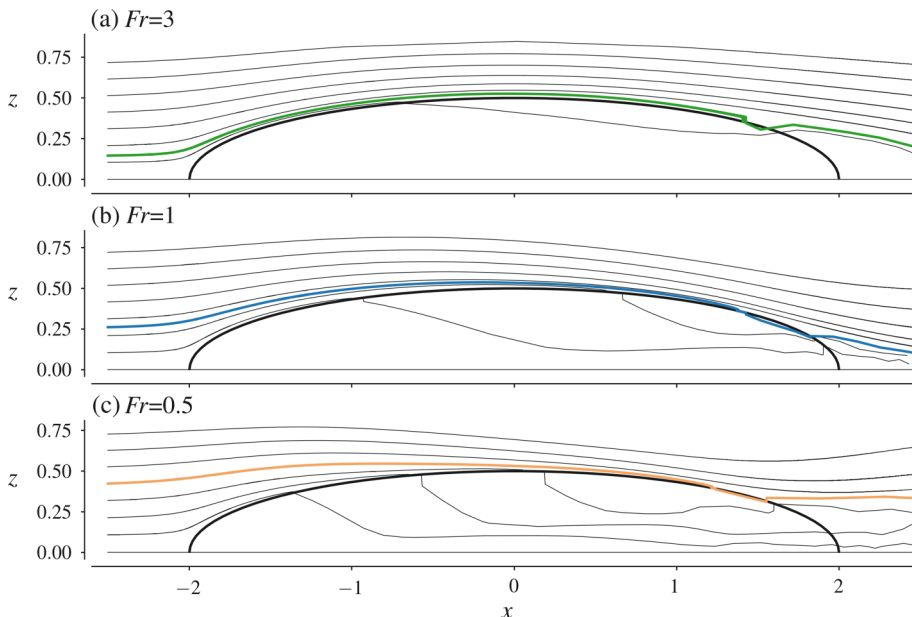


FIG. 9. Projection of a group of instantaneous isopycnals and the spheroid onto the vertical plane is shown: (a) $Fr = 3$, (b) $Fr = 1$, and (c) $Fr = 0.5$. The colored isopycnal serves as a surrogate for the dividing streamline.

the center line, since fluid is not prevented by buoyancy from going over or below the obstacle. As Fr decreases, the suppression of vertical motions increases so that the upper dividing surface moves upward. The dividing surface at $Fr = 0.5$ [Fig. 9(c)] is higher than that at $Fr = 1$ and $Fr = 3$ [Fig. 9(b)], but neither of the three simulated cases correspond to the $Fr \ll 1$ limit where the dividing surface reaches the half-height of the body.

It is worth noting that the piercing of the isopycnals starts from the aft of the body and that the separating stream surface is not horizontal. This small slope of the separating stream surface has been previously reported by Dalziel *et al.* [53] in the case of flow over a hemisphere, and is produced by the pressure difference that exists between the forebody and the aft. It has been shown to be relevant for the structure of the waves and to have a minor effect on the direction at which energy radiates from the body. The tilt of the dividing stream surface, and the location at which the flow starts being vertically constrained to go sideways and around the spheroid, are also reflected in the boundary layer evolution and the topology of flow separation as described below.

C. Boundary layer

The boundary layer (BL) on slender bodies and its separation has been extensively studied [5,6,62–64]. However, stratification effects on BL growth and separation on a slender body have received scant attention and will be discussed in this section.

To quantify the impact of buoyancy on the BL, the streamwise evolution of the displacement thickness (Δ) is computed at different Froude numbers and shown in Fig. 10. In nondimensional form, Δ is defined as

$$\Delta = \int_0^\infty \left(1 - \frac{u_t}{U_o}\right) dn, \quad (19)$$

where u_t is the wall-tangential velocity, U_o is the outer flow velocity, and n is the wall-normal distance coordinate. Note that Δ is normalized by the viscous length scale $D/Re^{1/2}$ to obtain $O(1)$ values.

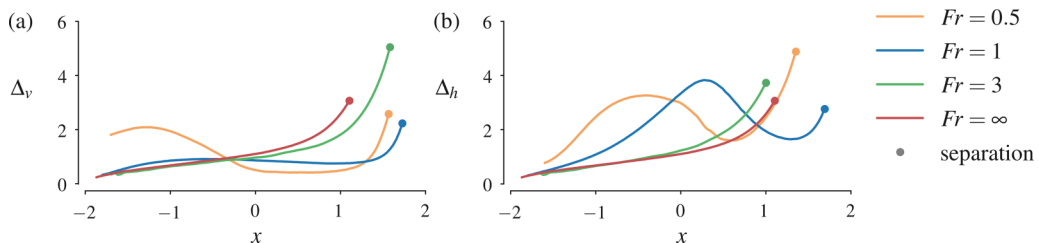


FIG. 10. Effect of Fr on the evolution of the boundary-layer displacement thickness: (a) in the central vertical plane (Δ_v) and (b) in the central horizontal plane (Δ_h). Dots show the separation locations.

In the $Fr = \infty$ case, shown as a red line in Fig. 10, the displacement thickness ($\Delta = \Delta_v = \Delta_h$) monotonically increases due to the viscous losses near the wall. Buoyancy induces azimuthal anisotropy on the evolution of the BL displacement thickness Δ [Eq. (19)] in contrast to the axisymmetric BL evolution in the unstratified case. Thus the normalized BL thickness in the vertical center plane Δ_v [Fig. 10(a)] at a given x is not equal to the corresponding measure in the horizontal center plane [Fig. 10(b)].

In the vertical plane [Fig. 10(a)], buoyancy reduces Δ_v in the rearward region of the body prior to the increase that precedes separation. In the forebody, relative to the unstratified counterpart, the weakly stratified $Fr = 3$ case behaves similarly, the moderately stratified $Fr = 1$ case shows a slight increase in Δ_v , while the $Fr = 0.5$ case exhibits a significant increase of Δ_v . This increase is associated with the blocking of the flow near the nose that leads to a thickening of the layer of low-momentum fluid. The three factors that contribute to the aforementioned effects in the vertical plane are (1) IGW, (2) body curvature, and (3) vertical flow confinement.

The nature of the IGW field was discussed in Sec. V. The closeup of the wave near field shows that the waves induce a change of sign of w [Fig. 6(c)]. The location where this change of sign occurs can be estimated as the intersection of the phase line passing through the center of the body with the surface of the body. The location of this intersection, which depends on the angle θ [Eq. (10)], marks the beginning of a region with inward near-body flow that helps the BL thin, so that Δ_v reduces with respect to the unstratified case.

The influence of body curvature and buoyancy was discussed in Sec. VIA to describe the force coefficients. A fluid parcel that climbs up the body “feels” gravity through $b_t = \mathbf{b} \cdot \mathbf{t}$ that is tangential to the surface and through the surface-normal component $b_n = \mathbf{b} \cdot \mathbf{n}$. In the forebody, b_t reduces the magnitude of acceleration that the flow normally experiences due to curvature causing the BL thickness to increase. The component b_n , however, tends to reduce Δ_v . At the nose, the effect of the tangential component dominates and the BL thickness increases as observed in Fig. 10(a) for $Fr = 1$. As the flow reaches a flatter part of the body, the normal component of buoyancy becomes more important and Δ_v tends to decrease. In the aft of the spheroid, both b_t and b_n act in tandem to decrease Δ_v .

Finally, vertical confinement and upstream blocking, that were discussed in Sec. VIB, also play a major role on BL evolution. Owing to vertical confinement, the near-body flow is able to follow the body curvature in the vertical plane for only a fraction of the half-height. Instead, it is deflected towards the sides of the body and downward. This feature contributes to the reduction of Δ_v .

The behavior of the BL thickness in the horizontal central plane with decreasing Fr is qualitatively different from that in the vertical, as can be seen upon comparison of Fig. 10(b) with Fig. 10(a). In the forebody, buoyancy tends to increase Δ_h . However, the evolution of Δ_h at the center and the aft of the body is more complex. At $Fr = 3$, Δ_h monotonically increases with increasing x . At $Fr = 1$ and $Fr = 0.5$, however, there is a region where Δ_h exhibits a strong decrease before commencing the pre-separation increase.

The behavior of the BL in the horizontal plane can be understood as the flow response to two flow features that have been discussed, namely, vertical confinement and IGW. The vertical confinement

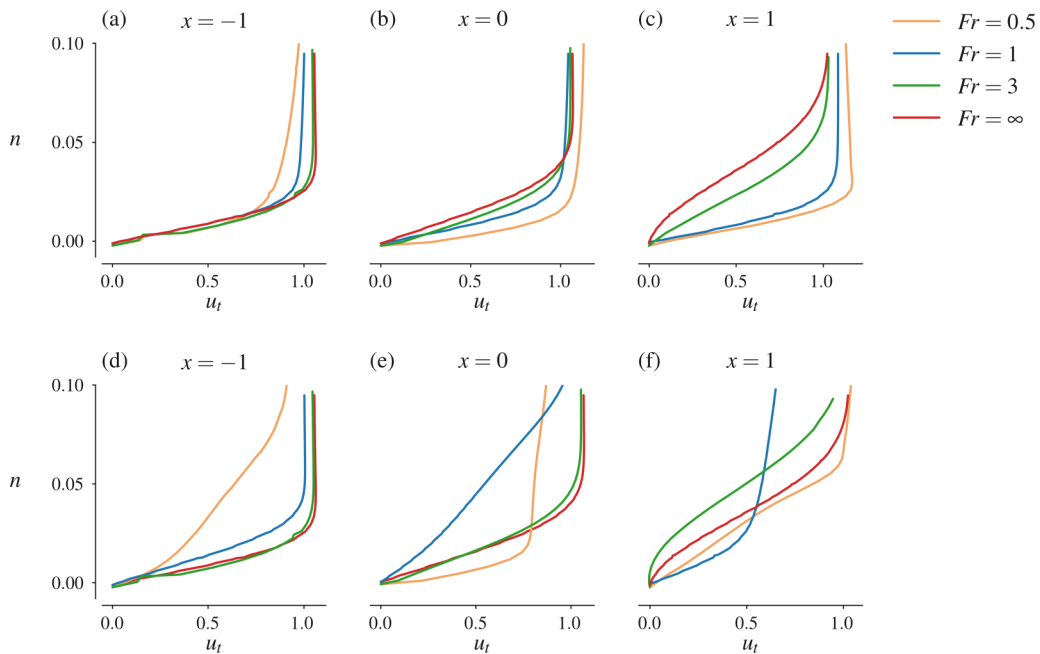


FIG. 11. Effect of Fr on the BL velocity profiles along the vertical (top row) and horizontal (bottom row) planes. The velocity is shown as a function of the nondimensional normal distance to the wall, n . Different streamwise locations are shown: left column corresponds to $x = -1$, middle column to $x = 0$, and right column to $x = 1$.

leads to deflection of the flow from the vertical towards the horizontal plane. This redirection of the flow enhances the growth of Δ_h . In the weakly stratified $Fr = 3$ case, it leads to a monotone increase of Δ_h [Fig. 10(b)] as is also evident from vorticity visualization. In the more stratified $Fr = 1$ and $Fr = 0.5$ cases, the vertical confinement is stronger and the fluid that goes around the body leads to a large increase of Δ_h .

After this rapid increase of the BL thickness as the flow traverses the forebody, the evolution of Δ_h exhibits a streamwise decrease that commences at a stratification-dependent location. In the $Fr = 1$ case, the decrease of Δ_h occurs at $x \approx 0.25$. However, at $Fr = 0.5$, this reversal of BL growth occurs at a much shorter distance from the nose, $x \approx -0.5$. The reversal of BL growth is caused by the response of the flow in the horizontal plane to the body-generated gravity wave. At $Fr = O(1)$, the IGW influence the near-body flow through the impressed radial velocity and the induced favorable pressure gradient in the rear part of the body. Indeed, the increase and subsequent decrease of Δ_h before the preseparation increase can be viewed as an oscillatory modulation of the BL thickness by the oscillatory wave.

The effect of stratification on the BL can be further clarified through the BL velocity profiles. Figure 11 shows profiles of tangential velocity (u_t) at different positions along the body surface in the vertical (top row) and horizontal (bottom row) planes. At $x = -1$, Fig. 11(a) shows minor differences among $Fr = 1, 3$ and ∞ in the vertical plane. Only the $Fr = 0.5$ case shows low-momentum fluid over a thicker region consistent with the substantially larger Δ_v shown in Fig. 10. Figure 11(b) shows that, already by $x = 0$, the BL in the stratified cases is thinned in the vertical by the normal component of the buoyancy force. The BL thinning is more pronounced further downstream as observed at $x = 1$ [Fig. 11(c)].

The thickening of the horizontal BL can also be observed in the BL profiles (bottom row of Fig. 11). Using the unstratified case as a reference, Fig. 11(d) shows that the BL profiles for the

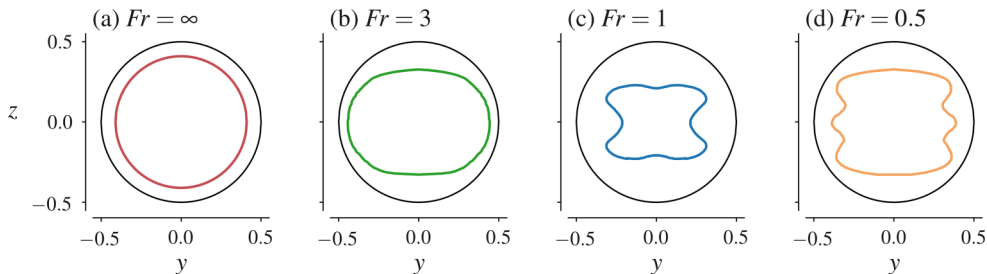


FIG. 12. Rear view of the prolate spheroid showing the effect of the stratification on the time-averaged separation line.

$Fr = 0.5$ and $Fr = 1$ cases are thicker at $x = -1$. At $x = 1$, Fig. 11(f), the $Fr = 3$ BL is separated. The $Fr = 0.5$ BL, which was substantially thicker than its unstratified counterpart at $x = 0$, has thinned to approach the unstratified thickness and the $Fr = 1$ BL is the thinnest of all. Notice how the change in the shape of the horizontal BL profiles at $Fr = 0.5$ between $x = -1$ and $x = 0$ is the same change experienced by the BL at $Fr = 1$ between $x = 0$ and $x = 1$. This reinforces the preceding argument that it is essentially the same mechanism, the interaction with the body-generated internal wave, that is operative in both cases to modulate the BL thickness.

D. Separation

The strong effect of buoyancy on the BL substantially affects flow separation. The line defined by connecting the points where $C_f = 0$ is an estimate of the location where the laminar BL separates from the body. The projection of this line on the back of the spheroid is shown in Fig. 12.

In the $Fr = \infty$ case, where there is no vertical density gradient in the flow, there is no preference among azimuthal directions. Therefore, on average, separation occurs at the same radial location for any azimuth and the separation line is a circle [Fig. 12(a)].

At the relatively mild stratification of $Fr = 3$, the circle deforms into an ellipse. The vertical confinement of the flow, albeit weaker than in the other stratified cases, promotes sideways motion and flow detachment in the horizontal plane, while the restoring force of buoyancy retards the separation in the vertical. When stratification is further increased to $Fr = 1$ and $Fr = 0.5$, there is a major qualitative change in the topology of the separation line as elaborated below.

As described in the previous section, the body-tangential component of buoyancy causes the flow to accelerate in the aft of the body. The increase in flow speed reduces the pressure on the tail sufficiently at $Fr = 1$ so that the flow in the horizontal plane remains attached for a long rearward portion of the body. The increase in attachment length is particularly pronounced in the central horizontal plane leading to the inward displacement of the separation line in the neighborhood of $z = 0$ [Fig. 12(c)].

When the Froude number is further reduced to $Fr = 0.5$, the separation region becomes larger instead of the shrinkage observed at $Fr = 1$. The strong difference between the $Fr = 1$ and $Fr = 0.5$ separation location can be attributed to the resonance between the spheroid and the lee waves. This resonant interaction was pointed out by Hunt and Snyder [26] in the case of submerged topography (a 3D hill), and by Hanazaki [22] and Chomaz *et al.* [24] in the case of the sphere, although at lower Re than in the present series. In the near field, discussed in Sec. V A, the body of length L forces an oscillatory response of the flow given by the wavelength $2L$. According to linear theory, discussed in Sec. V B, the oscillatory response of the far field is determined by the buoyancy frequency, the freestream velocity, and the body diameter as $\lambda/D = 2\pi U/ND = 2\pi Fr$. A critical Fr_c can be defined when the IGW half-wavelength ($\lambda/2$) coincides with the body length (L) leading to $Fr_c = L/D\pi$. At $Fr \approx Fr_c$, the lee-wave response matches the body shape leading to the maximal

suppression of separation, and the entry of the flow into the resonant or saturated lee wave (SLW) regime.

In the case of the sphere, low-Re studies of the SLW regime show that the lee wave is able to totally suppress separation when $Fr \approx Fr_c$. The simulations of Hanazaki [22] and the experiments of Chomaz *et al.* [24] show suppressed separation and a laminar wake at $Fr = 0.45$ and $Fr = 0.5$, respectively. Both values are near the critical value of $Fr_c = 1/\pi$ for the sphere. In the case of the 4:1 spheroid at $Re = 10^4$, when $Fr = 1 \approx Fr_c = L/D\pi = 4/\pi$, the steady lee wave is also sufficiently strong to lock in the wake and keep it steady and laminar.

When $Fr \gtrsim Fr_c$, there is inhibition of turbulence as was observed in the visualization of Fig. 4 and will be quantified later in Sec. VII. When $Fr \lesssim Fr_c$, such as the spheroid at $Fr = 0.5$, the lee-wave response induces earlier separation [see the positive w region right in the back of the body in Fig. 6(a)] and the separated region is enlarged [Fig. 12(d)]. Wake turbulence is reestablished at $Fr \lesssim Fr_c$, since the steady lee wave is not sufficiently strong to lock in the wake and the deflection of the flow towards the horizontal creates different flow features susceptible to instability, e.g., strong horizontal shear at the sides of the body.

In the case of a sphere, the deformation of the separation line has been demonstrated in laboratory experiments by Chomaz *et al.* [24,25]. By varying the Reynolds and the Froude numbers, they find that buoyancy results in three different topologies of the mean separation line: at high Froude number ($Fr \gtrsim Fr_c$), the line describes an ellipse whose minor axis is vertical; at low Froude number ($Fr \lesssim Fr_c$) or the 2D case, the fluid is vertically confined generating a square-shaped separation line; finally, in the SLW state ($Fr \approx Fr_c$), the shape of the separation line exhibits a strong Re dependence. At Re of the order of the steady-unsteady wake transition ($Re \approx 200$), the flow remains completely attached and the separation line degenerates to a point at the back of the body. At a slightly higher Re, the horizontal separation abruptly changes and a bowtie/peanut separation shape appears. This shape appears because at higher Re the flow in the horizontal plane separates at 90° (measured from the nose), while in the vertical plane the flow remains attached far longer to a location closer to 180° [25]. This bowtie shape has also been found in numerical simulations of a sphere wake [20].

In the spheroid case, the elongated horizontal axis of the body leads to a Fr-dependent deformation of the separation line that is different with respect to the sphere. The panels of Fig. 12 span $Fr \gtrsim Fr_c$ for the spheroid. They show that, as stratification increases, the separation location of the vertical and the horizontal planes is modified in a more correlative manner than in the bluff body case. Instead of the bowtie shape observed in the sphere [25] at similar conditions, the $Fr = 1$ and 0.5 cases for the spheroid show that flow separation in the vertical and horizontal planes occurs approximately at the same angle measured from the nose.

Figure 13 illustrates the lee-wave induced pressure field in the vertical plane. Together with Fig. 6, which showed the lee-wave induced vertical velocity w (Sec. VB), it provides a full picture of the influence of the IGW on the separation of the BL. In the $Fr = 1$ case, the IGW field presents a wide region of low pressure in the back of the body Fig. 13(b), where the vertical velocity w of the IGW is negative [Fig. 6(c)]. Both features cause the reduction of the BL separation and the establishment of a laminar wake. However, at $Fr = 0.5$ the opposite effect is observed. The low-pressure region in the back of the body is smaller and the pressure gradient weaker [Fig. 13(a)], the vertical velocity induced in the rear part of the body is positive [Fig. 6(a)], and the IGW enlarges the separation region.

To elucidate the influence of the aspect ratio, Fig. 13 also compares the pressure contours of the present simulations with the pressure contours of a $Re = 3700$ flow past a sphere. Among the cases shown, the sphere with $Fr = 1$ and the spheroid at $Fr = 0.5$ have wake instabilities and turbulence. In contrast, the sphere with $Fr = 0.5$ and the 4:1 spheroid at $Fr = 1$ are cases where the Fr is sufficiently close to the critical value ($Fr_c = L/D\pi$) required to establish a SLW specific to each body shape. In the SLW state, the favorable pressure gradient is sufficiently strong to prevent transition to turbulence. There is possibly an effect of body Re, and it remains to be seen if the

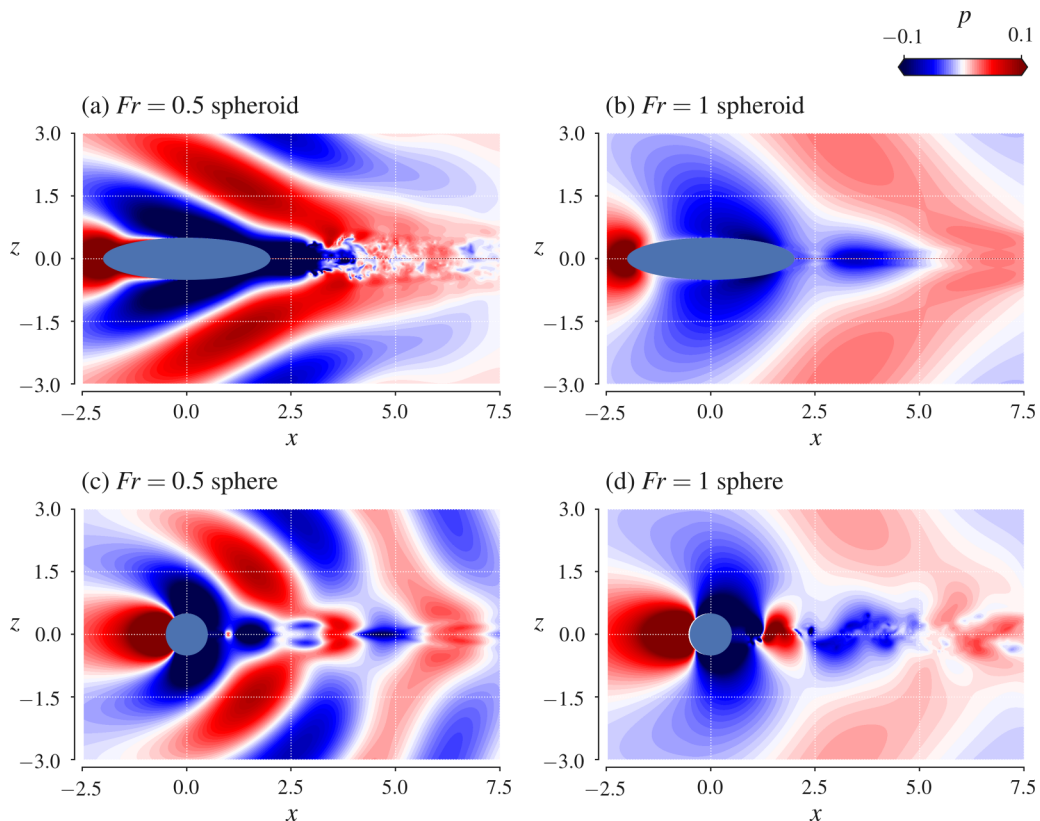


FIG. 13. Instantaneous pressure fields. Top row shows spheroid at $Re = 10^4$: (a) $Fr = 0.5$ and (b) $Fr = 1$. Bottom row shows sphere at $Re = 3700$: (c) $Fr = 0.5$ and (d) $Fr = 1$.

absence of wake turbulence found here for the $Fr = 1$ spheroid persists at higher values of local wake Reynolds number.

VII. WAKE

The effects of stratification on the flow at the body ultimately affect the establishment of the wake and its downstream evolution. This section describes the structure and the decay of the near and intermediate wake by looking into its size, energy, and frequency content.

In the discussion, the results are often contrasted with previous findings on the wake of the sphere to elucidate the role of the wake-generator shape. An overall finding is that, for the same value of Fr , the 4:1 spheroid exhibits a stronger effect of buoyancy than the sphere.

Figures 14(a) and 14(b) show the evolution of the wake half-thickness defined as the radial distance where the mean defect velocity, $U_d = U - \bar{u}$, is half of its center line value. In the stratified cases, the magnitude of the half-thickness depends on the azimuthal location and we will refer to its vertical value as half-height L_V and its horizontal value as half-width L_H . The dimensions of the near wake are directly correlated with the size and shape of the separated region. Figures 14(a) and 14(b) show that, using as a reference the neutral case, the $Fr = 3$ wake is shorter and wider, the $Fr = 1$ wake is the thinnest of all, and the $Fr = 0.5$ wake is the thickest.

In the case of $Fr = 1 \approx Fr_c$, the wake is in the SLW state. In this regime, the steady lee wave dominates the wake evolution so that the wake is steady and the thickness growth rate is relatively small. The oscillations in the wake height are opposed in phase with respect to the wake width and

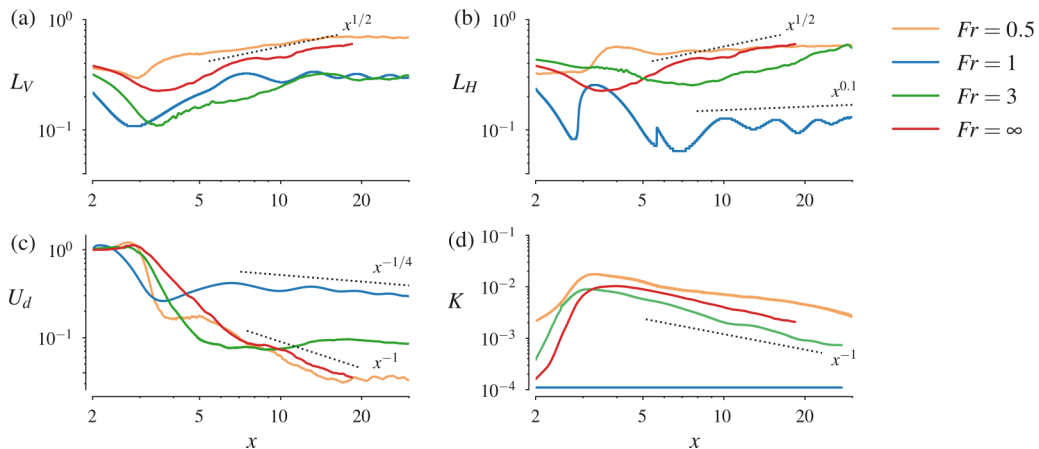


FIG. 14. Effect of stratification on the streamwise evolution of overall wake properties: (a) half-height (L_V), (b) half-width (L_H), (c) center line defect velocity (U_d), and (d) turbulent kinetic energy (TKE).

they oscillate with a wavelength of $\lambda/D = 2\pi Fr$. This oscillatory modulation is weaker for both $Fr = 3 > Fr_c$ and $Fr = 0.5 < Fr_c$ cases.

At $Fr = 3$ and $Fr = 1$, the wake height saturates around $L_V \approx 0.3$, which coincides with the result of Pal *et al.* [12] for a sphere. At $Fr = 0.5$, L_V saturates at ≈ 0.7 . This larger value is caused by the earlier flow separation induced by the lee wave, as was described in the preceding section. Although the wake height (L_V) saturates, the wake width (L_H) keeps growing. In the $Fr = 3$ wake, we observe a growth slightly larger than the unstratified counterpart of $L_H \propto x^{1/2}$. In the $Fr = 1$ and $Fr = 0.5$ cases, however, the growth rate is found to be low, $L_H \propto x^{0.1}$.

Figure 14(c) shows the evolution of U_d along the streamwise direction. Once buoyancy effects have set in, the defect velocity U_d in stratified wakes is larger than in unstratified wakes. Owing to this feature, stratified wakes are said to have a “longer lifetime” relative to their unstratified counterpart. The decay of U_d in the nonequilibrium regime is similar between $Fr = 1$ and $Fr = 3$ cases, and is close to $U_d \propto x^{-0.22} \approx x^{-1/4}$, consistent with previous findings for the sphere [9,10]. The decay also shows the imprint of the lee wave oscillations. At $Fr = 0.5$, the value of U_d initially decays at a higher rate than its unstratified counterpart. Between $x = 5$ and 20, $U_d \propto x^{-1}$ is similar to the unstratified case and, only after $x = 20$, the decay rate exhibits the flattening trend that was observed at larger Fr . In the case of $Fr = 0.5$, the imprint of the oscillatory modulation is only observed in this later region.

In the unstratified wake, the decay rate of the defect velocity is close to $U_d \propto x^{-0.98} \approx x^{-1}$ and the growth of the wake thickness is close to $L_H = L_V \propto x^{0.48} \approx x^{1/2}$. These power-law exponents should not be misinterpreted as the low-Re scaling [65], since the Reynolds number chosen in this work is not small. The mean-field dissipation is much smaller than the turbulent production in the mean kinetic energy equation and the Reynolds number ($Re_\lambda = u_{rms} l_T / \nu$) based on the Taylor microscale (l_T) is $O(100)$, showing that the wake is not laminar. The power laws are established at $x \approx 8$, similar to the location where the sphere of Pal *et al.* [12] at $Re = 3700$ started showing the same power laws.

Relative to the sphere, the difference in the near wake between the moderately stratified $Fr = 3$ and the unstratified $Fr = \infty$ cases is substantially stronger for the 4:1 spheroid. In the case of a sphere at $Fr = 3$ and $Re = 10^4$, the evolution of U_d is identical between $Fr = 3$ and $Fr = \infty$ until $x \approx 6$ or $Nt \approx 2$ [48]. In contrast, the spheroid wake deviates from its unstratified counterpart much closer to the body, $x \approx 2-3$, as can be seen from the evolution of defect velocity [Fig. 14(b)], the vertical contraction of the postseparation shear layer (Fig. 4), and the wake-thickness anisotropy, which is visible right behind the body [Fig. 14(a)]. Thus it is evident that the minimum Froude

number that must be exceeded for the spheroid to exhibit the 3D regime (near wake that is nominally unstratified [9]) is larger than the minimum Fr for a sphere. Since slender bodies present smaller recirculation regions than bluff bodies (they have wakes with lower turbulent production [66] and lower local $Re_d = U_d L_V / \nu$ for the same body Re) it might be tempting to think that, owing to lower local Re , the turbulence “feels” gravity effects closer to the body. However, a close comparison of the present results with those of a sphere at $Re = 10^4$ and $Fr = 3$ of Chongsiripinyo and Sarkar [48] reveals that the buoyancy Reynolds number ($Re_b = \varepsilon / \nu N^2$) at the same x locations takes similar values in the sphere and the spheroid wakes. This suggests that the present finding of the nonexistence of a 3D, unstratified regime behind the spheroid at $Fr = 3$ is not a lowering of Re_b in the spheroid wake. It is rather because the interaction of the near wake with the body-generated lee wave is stronger for the spheroid than for the sphere.

To quantify the impact of background stratification on the turbulent behavior of the wake, Fig. 14(d) shows the evolution of turbulent kinetic energy (TKE), $K = \frac{1}{2} \overline{u_i' u_i'}$, integrated over the domain cross section ($0 \leq dr \leq L_r$, $0 \leq d\Theta \leq 2\pi$).

Figure 14(d) shows that, as Fr decreases, the TKE in the intermediate wake tends to decrease with respect to the unstratified value until at $Fr = 1 \approx Fr_c$ it becomes negligible. A remarkable result is that, upon further decrease of Fr to $0.5 < Fr_c$, TKE increases to a value that is even larger than in the unstratified case. In the unstratified case, the TKE evolution shows a peak at $x \approx 4$, which corresponds to the end of the recirculation region [see Fig. 4(a)]. In the $Fr = 3$ case, the recirculation region ends at $x \approx 3$ [Fig. 4(b)], closer to the body, due to the vertical confinement by buoyancy and the modified separation topology. Accordingly, the peak TKE is also at $x \approx 3$. Regarding the TKE evolution, the $Fr = 3$ case shows a slightly faster decay than the unstratified case. The $Fr = 0.5$ wake also shows a peak followed by a decrease, but in this case K is significantly larger than in the other cases throughout the domain.

As was previously mentioned, the $Fr = 1$ wake is steady, laminar, and thinner than taller ($L_H < L_V$), as is evident from comparison of Figs. 14(a) and 14(b). The shape of the wake is shown at various streamwise locations with more detail in Fig. 15. This configuration had not been reported before in the literature and it is remarkable, since stratification is associated with vertical confinement of the wake, and it normally leads to $L_H > L_V$ wakes. Initially, the $L_H < L_V$ feature in the $Fr = 1$ wake is caused by the different body type (slender instead of bluff) that leads to a different IGW effect on flow separation. Further downstream, it is the lack of turbulent mixing that keeps the wake from rapidly transitioning to a $L_H > L_V$ configuration.

Spectra

Apart from introducing N as a natural frequency of the flow, and causing the oscillatory modulation of the wake, stratification and buoyancy also lead to changes in vortex shedding from the body. Consequently, there are changes in the frequency of the dominant modes in the velocity spectra.

Figure 16 shows the energy spectrum (E_{uu}) obtained from the time series of streamwise velocity (u) at different locations in the wake. The energy content is shown as a function of the nondimensional frequency or Strouhal number (St). Here, $St = fD/U$, where the dimensional f is in cycles per second. At $Fr = \infty$ [Fig. 16(a)], E_{uu} at $x = 4$, a location at the end of the recirculation region, shows a peak at $St \approx 0.59$, which coincides with the value reported by Tezuka and Suzuki [67] for the same body at $Re = 7 \times 10^3$. The value of $St \approx 0.59$ corresponds to the $m = 1$ vortex shedding mode associated with the helicoidal shape of the unstratified wake, which was presented in Fig. 1. Moving downstream, the spectral peak associated with the shedding frequency is less noticeable as a discrete peak in the spectrum since the energy gets distributed among more frequencies.

At $Fr = 3$ [Fig. 16(b)], the vortex shedding peak at $St = 0.59$ is observed at $x = 6$ but is not prominent at locations further downstream. In the horizontal plane (not shown), E_{uu} at $Fr = 3$ does not reveal any characteristic shedding frequency, which is consistent with the visualization of Fig. 5(a) that shows horizontal broadband structures without a dominant mode.

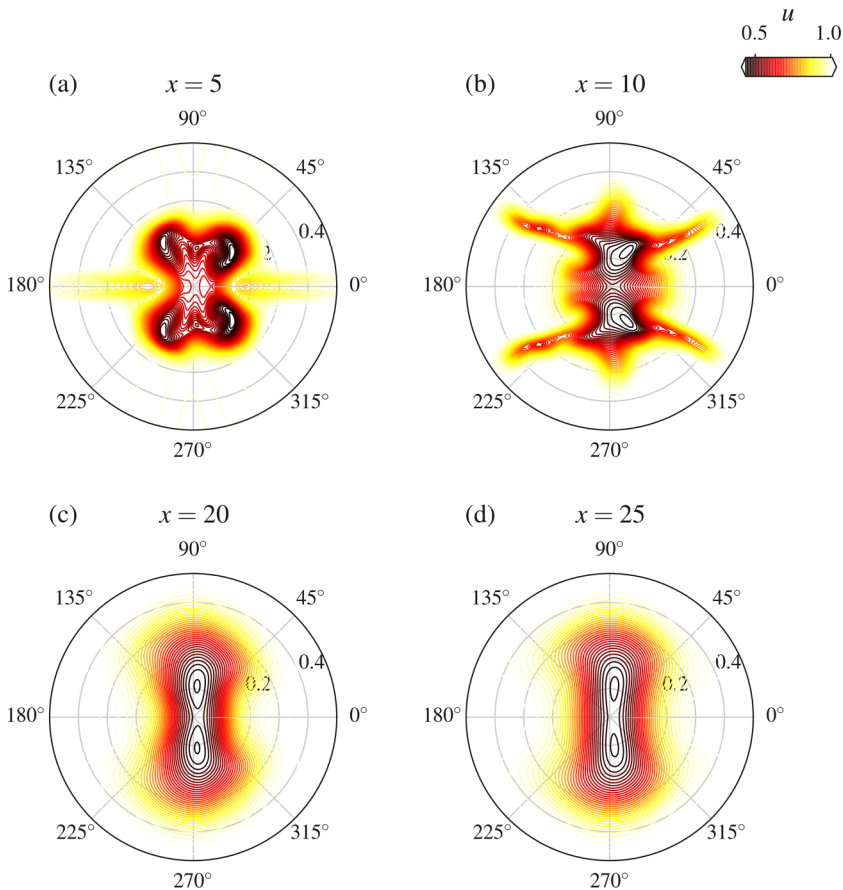


FIG. 15. Azimuthal planes of streamwise velocity in the $Fr = 1$ wake at different streamwise locations. Note that the $Fr = 1$ wake is steady and the flow is close to the resonant condition of $Fr = Fr_c$.

In the strongly stratified $Fr = 0.5$ case, E_{uu} at $x = 6$ [Fig. 16(c)] shows a peak at $St = 0.33$, which is lower than the frequency peak ($St = 0.59$) at $Fr = \infty$. The spectrum also shows a secondary peak at $St = 2$ that corresponds with the buoyancy frequency N . The differences in spectra between the $\Theta = 45^\circ$ [Fig. 16(c)] and horizontal planes [Fig. 16(d)] at $Fr = 0.5$ reveal the azimuthal anisotropy of the flow. This observation is consistent with the change of wake instability induced by stratification. As stratification is increased, the three-dimensional helical structure observed at $Fr = \infty$ is altered so that there is a significant wavy component in the horizontal plane [Fig. 5(d)] but not in the vertical plane [Fig. 5(d)]. Therefore, Fig. 16(d) shows a substantial peak at $St = 0.4$ for $\Theta = 0^\circ$ but not for $\Theta = 90^\circ$.

VIII. SUMMARY AND CONCLUSIONS

The present work examines stratified turbulent flow past a 4:1 prolate spheroid. The aim is to elucidate the role that the aspect ratio greater than one ($L/D > 1$) has in the way that buoyancy alters the flow. Unlike previous studies, which focus primarily on flow past spheres, the present analysis describes the influence of the slenderness of the body on the structure of the internal gravity waves (IGW), the evolution of the boundary layer, flow separation, and the near-to-intermediate wake. A highly resolved large-eddy simulation (LES) is conducted wherein the Navier-Stokes equations under the Boussinesq approximation are solved in a cylindrical grid. The Reynolds number based

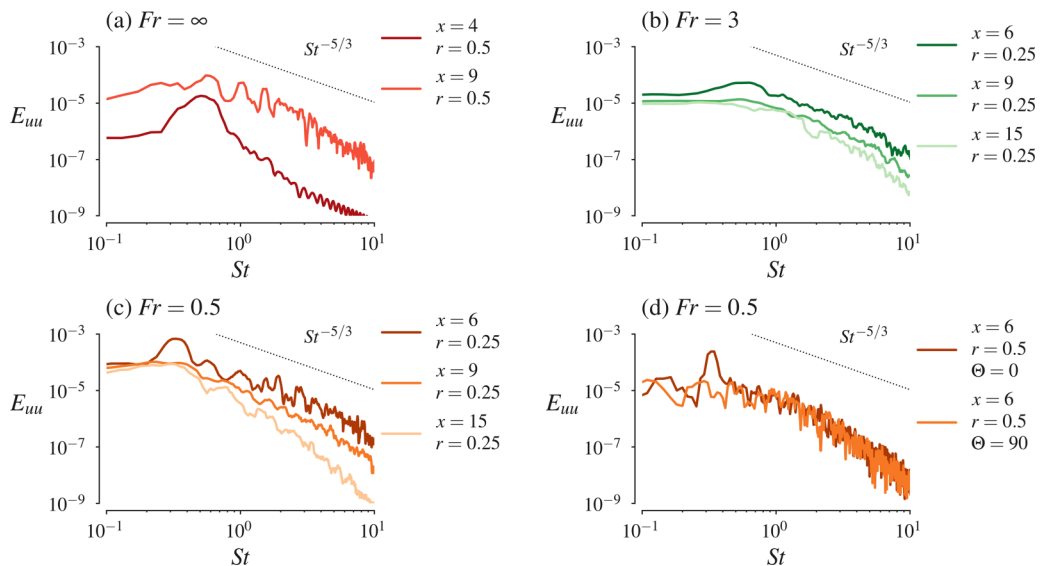


FIG. 16. Energy spectra, as a function of Strouhal number (St), computed from the time series of streamwise velocity at different locations. The quantity St is the nondimensional frequency, $St = fD/U$, where the dimensional f is in cycles per s. The azimuthal location of the velocity probes of (a), (b), and (c) is $\Theta = 45^\circ$, while (d) corresponds to probes located in the horizontal ($\Theta = 0^\circ$) and the vertical ($\Theta = 90^\circ$) direction.

on the minor axis (D) is set to $Re = UD/\nu = 10^4$ and the level of stratification is changed so that the Froude number is $Fr = U/ND = 0.5, 1, \text{ and } 3$. The unstratified ($Fr = \infty$) case is also simulated.

At the same value of Fr , the spheroid exhibits a stronger effect of buoyancy than the sphere. This is caused by the interaction of the IGW, which has a characteristic wavelength $\lambda = 2\pi U/N$ with the body major axis L . Based on this interaction, a critical Froude number (Fr_c) can be defined at which the half-wavelength of the IGW matches the body length. Imposing $\lambda/2 = L$ leads to $Fr_c = L/D\pi$ as the criterion for the saturated lee wave (SLW) regime. When $Fr \approx Fr_c$, the delay of flow separation caused by the IGW is maximal, and the turbulent kinetic energy in the wake becomes minimal. When $Fr \gtrsim Fr_c$, stratification partially suppresses the turbulence in the wake. However, when $Fr \lesssim Fr_c$, the IGW induce earlier separation and the turbulent kinetic energy in the subsequent wake is larger than under unstratified conditions. The simulations of Pal *et al.* [19] at $Re = 3700$ showed that the wake of a sphere is laminar at $Fr = 0.5 \approx Fr_c = 1/\pi$, turbulent at $Fr = 1 > Fr_c$, and turbulent at $Fr = 0.25 < Fr_c$. The present simulations show that the 4:1 spheroid wake at $Re = 10^4$ is laminar at $Fr = 1 \approx Fr_c = 4/\pi$, turbulent at $Fr = 3 > Fr_c$, and turbulent at $Fr = 0.5 < Fr_c$. The SLW regime had been previously identified for a sphere at low Re [22,24] and for flow past a 3D hill [26], but here we report the SLW regime and its influence on the wake for a slender body.

The modification of flow separation by buoyancy is mainly caused by the imprint of the IGW on the vertical velocity and on the pressure gradient at the back of the body. To find the dependence of the IGW far field on the aspect ratio, L/D , the present work uses linear theory and adapts the asymptotic work of Voisin [34] for a sphere to the prolate spheroid. In the far field, the actual shape of the body loses significance, although it is necessary to account for its finite size to be able to match the location of the phase lines observed in the simulation. The tilting of the IGW phase lines in the near field depends on the body aspect ratio and a theoretical estimate of the tilt is obtained.

Apart from exploring the influence of the aspect ratio on the IGW, the present work includes a detailed description of the flow at the body: the pressure and friction coefficients are computed as a function of the Froude number to explain the increase in the drag force with stratification, the

blocking effects in the nose are quantified using the separating streamline of Drazin [61], and the evolution of the boundary layer is compared between the vertical and horizontal planes. The flow features induced by stratification can be understood as a result of three main effects: (1) the interaction of the buoyancy force with the body curvature, (2) the vertical velocity induced by the IGW in the near field, and (3) the upstream blocking and vertical confinement experienced by the flow which forces fluid to move sideways instead of directly above or below the body.

To understand the relevance of these effects on the wake establishment, the topology of the separation line is described and compared with the separation of the sphere. A general observation is that, as opposed to the sphere, the separation of stratified flow at the spheroid occurs at a similar radial location in the vertical and horizontal planes. The type of separation strongly influences the dimensions, the decay rate, and the turbulent kinetic energy of the near wake.

Generally, stratified wakes are thought to be wider than taller, since the flow is vertically confined by stable stratification. However, in the present simulations, the $Fr = 1$ and $Fr = 0.5$ wakes show a taller than wider configuration. This topology, which has not been reported in previous work on sphere wakes, is caused by the $L/D > 1$ geometry that has a different interaction with buoyancy.

The decay rate of the present stratified wakes is smaller than the unstratified wake, and they show a characteristic oscillatory modulation caused by the body lee waves. These observations are consistent with previous findings for wake decay [8] and oscillatory wake modulation [12]. The reappearance of wake turbulence at low Fr is also consistent with previous findings for the sphere wake [19], although the required Fr is shown here to depend on the body shape.

The present results can be employed in the future to provide inflow conditions for a spatial wake model and initial conditions for a temporal wake model. The flow around the body no longer needs to be simulated in these hybrid models [68]. Thus the wake evolution can be obtained in a cost effective way while taking advantage of the realism of the body inclusive simulations. Additionally, since the present results have been obtained at a moderate Re , we are considering stratified slender-body wakes at higher Re in ongoing work. This work will include a tripped, turbulent boundary layer to ascertain the robustness of the Fr dependence found here for flow past a spheroid.

ACKNOWLEDGMENTS

We gratefully acknowledge the support of ONR Grant No. N00014-15-1-2718 and the reviewers for their thorough and helpful comments. We are also pleased to acknowledge a two-year fellowship provided by La Caixa Foundation to J.L.O.-T. Computing time was provided through the DoD High Performance Computing Modernization Program (HPCMP).

-
- [1] K. C. Wang, Three-dimensional boundary layer near the plane of symmetry of a spheroid at incidence, *J. Fluid Mech.* **43**, 187 (1970).
 - [2] C. E. Costis, D. P. Telionis, and N. T. Hoang, Laminar separating flow over a prolate spheroid, *J. Aircr.* **26**, 810 (1989).
 - [3] C. J. Chesnakas and R. L. Simpson, Full three-dimensional measurements of the cross-flow separation region of a 6:1 prolate spheroid, *Exp. Fluids* **17**, 68 (1994).
 - [4] T. C. Fu, A. Shekarriz, J. Katz, and T. T. Huang, The flow structure in the lee of an inclined 6:1 prolate spheroid, *J. Fluid Mech.* **269**, 79 (1994).
 - [5] G. S. Constantinescu, H. Pasinato, Y. Q. Wang, J. R. Forsythe, and K. D. Squires, Numerical investigation of flow past a prolate spheroid, *J. Fluids Eng.* **124**, 904 (2002).
 - [6] N. Wikström, U. Svennberg, N. Alin, and C. Fureby, Large eddy simulation of the flow around an inclined prolate spheroid, *J. Turbul.* **5**, N29 (2004).
 - [7] J. T. Lin and Y. H. Pao, Wakes in stratified fluids, *Annu. Rev. Fluid Mech.* **11**, 317 (1979).
 - [8] G. R. Spedding, Wake signature detection, *Annu. Rev. Fluid Mech.* **46**, 273 (2014).

- [9] G. R. Spedding, The evolution of initially turbulent bluff-body wakes at high internal Froude number, *J. Fluid Mech.* **337**, 283 (1997).
- [10] K. A. Brucker and S. Sarkar, A comparative study of self-propelled and towed wakes in a stratified fluid, *J. Fluid Mech.* **652**, 373 (2010).
- [11] P. J. Diamessis, G. R. Spedding, and J. A. Domaradzki, Similarity scaling and vorticity structure in high-Reynolds-number stably stratified turbulent wakes, *J. Fluid Mech.* **671**, 52 (2011).
- [12] A. Pal, S. Sarkar, A. Posa, and E. Balaras, Direct numerical simulation of stratified flow past a sphere at a subcritical Reynolds number of 3700 and moderate Froude number, *J. Fluid Mech.* **826**, 5 (2017).
- [13] M. Bonnier and O. Eiff, Experimental investigation of the collapse of a turbulent wake in a stably stratified fluid, *Phys. Fluids* **14**, 791 (2002).
- [14] M. J. Gourlay, S. C. Arendt, D. C. Fritts, and J. Werne, Numerical modeling of initially turbulent wakes with net momentum, *Phys. Fluids* **13**, 3783 (2001).
- [15] D. G. Dommermuth, J. W. Rottman, G. E. Innis, and E. A. Novikov, Numerical simulation of the wake of a towed sphere in a weakly stratified fluid, *J. Fluid Mech.* **473**, 83 (2002).
- [16] M. B. De Stadler and S. Sarkar, Simulation of a propelled wake with moderate excess momentum in a stratified fluid, *J. Fluid Mech.* **692**, 28 (2012).
- [17] J. A. Redford, T. S. Lund, and G. N. Coleman, A numerical study of a weakly stratified turbulent wake, *J. Fluid Mech.* **776**, 568 (2015).
- [18] T. S. Orr, J. A. Domaradzki, G. R. Spedding, and G. S. Constantinescu, Numerical simulations of the near wake of a sphere moving in a steady, horizontal motion through a linearly stratified fluid at $Re = 1000$, *Phys. Fluids* **27**, 035113 (2015).
- [19] A. Pal, S. Sarkar, A. Posa, and E. Balaras, Regeneration of turbulent fluctuations in low-Froude-number flow over a sphere at a Reynolds number of 3700, *J. Fluid Mech.* **804**, R21 (2016).
- [20] K. Chongsiripinyo, A. Pal, and S. Sarkar, On the vortex dynamics of flow past a sphere at $Re = 3700$ in a uniformly stratified fluid, *Phys. Fluids* **29**, 020704 (2017).
- [21] P. Meunier and G. R. Spedding, A loss of memory in stratified momentum wakes, *Phys. Fluids* **16**, 298 (2004).
- [22] H. Hanazaki, A numerical study of three-dimensional stratified flow past a sphere, *J. Fluid Mech.* **192**, 393 (1988).
- [23] Q. Lin, W. R. Lindberg, D. L. Boyer, and H. J. S. Fernando, Stratified flow past a sphere, *J. Fluid Mech.* **240**, 315 (1992).
- [24] J. M. Chomaz, P. Bonneton, A. Butet, M. Perrier, and E. J. Hopfinger, Froude number dependence of the flow separation line on a sphere towed in a stratified fluid, *Phys. Fluids* **4**, 254 (1992).
- [25] J. M. Chomaz, P. Bonneton, and E. J. Hopfinger, The structure of the near wake of a sphere moving horizontally in a stratified fluid, *J. Fluid Mech.* **254**, 1 (1993).
- [26] J. C. R. Hunt and W. H. Snyder, Experiments on stably and neutrally stratified flow over a model three-dimensional hill, *J. Fluid Mech.* **96**, 671 (1980).
- [27] I. P. Castro, W. H. Snyder, and G. L. Marsh, Stratified flow over three-dimensional ridges, *J. Fluid Mech.* **135**, 261 (1983).
- [28] B. Voisin, Internal wave generation in uniformly stratified fluids. Part 2. Moving point sources, *J. Fluid Mech.* **261**, 333 (1994).
- [29] G. D. Crapper, A three-dimensional solution for waves in the lee of mountains, *J. Fluid Mech.* **6**, 51 (1959).
- [30] J. W. Miles, Internal waves generated by a horizontally moving source, *Geophys. Astrophys. Fluid Dyn.* **2**, 63 (1971).
- [31] I. V. Sturova, Wave motions produced in a stratified liquid from flow past a submerged body, *J. Appl. Mech. Tech. Phys.* **15**, 796 (1976) [translated from *Zh. Prikl. Mekh. Tekh. Fiz.* **3**, 61 (1976)].
- [32] G. S. Janowitz, Lee waves in three-dimensional stratified flow, *J. Fluid Mech.* **148**, 97 (1984).
- [33] P. Dupont and B. Voisin, Internal waves generated by a translating and oscillating sphere, *Dynam. Atmos. Oceans* **23**, 289 (1996).
- [34] B. Voisin, Lee waves from a sphere in a stratified flow, *J. Fluid Mech.* **574**, 273 (2007).

- [35] H. E. Gilreath and A. Brandt, Experiments on the generation of internal waves in a stratified fluid, *AIAA J.* **23**, 693 (1985).
- [36] P. Dupont, Y. Kadri, and J. M. Chomaz, Internal waves generated by the wake of Gaussian hills, *Phys. Fluids* **13**, 3223 (2001).
- [37] A. M. Abdilghanie and P. J. Diamessis, The internal gravity wave field emitted by a stably stratified turbulent wake, *J. Fluid Mech.* **720**, 104 (2013).
- [38] A. Brandt and J. R. Rottier, The internal wavefield generated by a towed sphere at low Froude number, *J. Fluid Mech.* **769**, 103 (2015).
- [39] Q. Zhou and P. J. Diamessis, Surface manifestation of internal waves emitted by submerged localized stratified turbulence, *J. Fluid Mech.* **798**, 505 (2016).
- [40] P. Meunier, S. L. Dizès, L. Redekopp, and G. R. Spedding, Internal waves generated by a stratified wake: Experiment and theory, *J. Fluid Mech.* **846**, 752 (2018).
- [41] M. B. de Stadler, S. Sarkar, and K. A. Brucker, Effect of the Prandtl number on a stratified turbulent wake, *Phys. Fluids* **22**, 095102 (2010).
- [42] M. Germano, U. Piomelli, P. Moin, and W. H. Cabot, A dynamic subgrid-scale eddy viscosity model, *Phys. Fluids A: Fluid Dyn.* **3**, 1760 (1991).
- [43] D. K. Lilly, A proposed modification of the Germano subgrid-scale closure method, *Phys. Fluids A: Fluid Dyn.* **4**, 633 (1992).
- [44] T. Rossi and J. Toivanen, A parallel fast direct solver for block tridiagonal systems with separable matrices of arbitrary dimension, *SIAM J. Sci. Comput.* **20**, 1778 (1999).
- [45] E. Balaras, Modeling complex boundaries using an external force field on fixed Cartesian grids in large-eddy simulations, *Comput. Fluids* **33**, 375 (2004).
- [46] J. Yang and E. Balaras, An embedded-boundary formulation for large-eddy simulation of turbulent flows interacting with moving boundaries, *J. Comput. Phys.* **215**, 12 (2006).
- [47] H. Lamb, *Hydrodynamics* (Cambridge University Press, Cambridge, UK, 1916).
- [48] K. Chongsiripinyo and S. Sarkar, Effect of stratification on the turbulent wake behind a sphere at $Re = 10,000$, 10th International Symposium on Turbulence and Shear Flow Phenomena, TSFP10 (Chicago, 2017).
- [49] P. G. Baines, *Topographic Effects in Stratified Flows* (Cambridge University Press, Cambridge, UK, 1998).
- [50] R. S. Scorer, Theory of waves in the lee of mountains, *Q. J. R. Meteorol. Soc.* **75**, 41 (1949).
- [51] R. B. Smith, Linear theory of hydrostatic flow over an isolated mountain in isosteric coordinates, *J. Atmos. Sci.* **45**, 3889 (1988).
- [52] C. J. Nappo, *An Introduction to Atmospheric Gravity Waves* (Elsevier Science, Amsterdam, 2002).
- [53] S. B. Dalziel, M. D. Patterson, C. P. Caulfield, and S. Le Brun, The structure of low-Froude-number lee waves over an isolated obstacle, *J. Fluid Mech.* **689**, 3 (2011).
- [54] B. Voisin, Limit states of internal wave beams, *J. Fluid Mech.* **496**, 243 (2003).
- [55] J. Pedlosky, *Waves in the Ocean and the Atmosphere* (Springer-Verlag, Berlin, 2003).
- [56] K. E. Lofquist and L. P. Purtell, Drag on a sphere moving horizontally through a stratified liquid, *J. Fluid Mech.* **148**, 271 (1984).
- [57] M. D. Greenslade, Drag on a sphere moving horizontally in a stratified fluid, *J. Fluid Mech.* **418**, 339 (2000).
- [58] P. J. Mason, Forces on spheres moving horizontally in a rotating stratified fluid, *Geophys. Astro. Fluid* **8**, 137 (1977).
- [59] P. K. Kundu, I. M. Cohen, and D. R. Dowling, *Fluid Mechanics*, 5th ed. (Academic Press, 2001), Vol. 40, p. 9823.
- [60] P. A. Sheppard, Airflow over mountains, *Q. J. R. Meteorol. Soc.* **82**, 528 (1956).
- [61] P. G. Drazin, On the steady flow of a fluid of variable density past an obstacle, *Tellus* **13**, 239 (1961).
- [62] T. Han and V. C. Patel, Flow separation on a spheroid at incidence, *J. Fluid Mech.* **92**, 643 (1979).
- [63] C. J. Chesnakas, D. Taylor, and R. L. Simpson, Detailed investigation of the three-dimensional separation about a 6:1 prolate spheroid, *AIAA J.* **35**, 990 (1997).
- [64] K. C. Wang, H. C. Zhou, C. H. Hu, and S. Harrington, Three-dimensional separated flow structure over prolate spheroids, *Proc. R. Soc. London, Ser. A: Math. Phys. Sci.* **429**, 73 (1990).

- [65] A. A. Townsend, *The Structure of Turbulent Shear Flow* (Cambridge University Press, Cambridge, UK, 1956).
- [66] R. Chevray, The turbulent wake of a body of revolution, [ASME J. Basic Eng.](#) **90**, 275 (1968).
- [67] A. Tezuka and K. Suzuki, Three-dimensional global linear stability analysis of flow around a spheroid, [AIAA J.](#) **44**, 1697 (2006).
- [68] A. VanDine, K. Chongsiripinyo, and S. Sarkar, Hybrid spatially-evolving DNS model of flow past a sphere, [Comput. Fluids](#) **171**, 41 (2018).